NAVAL POSTGRADUATE SCHOOL

MONTEREY, CALIFORNIA

THESIS

MULTI-CONJUGATE ADAPTIVE OPTICS PERFORMANCE IN SIMULATED ATMOSPHERIC DEEP TURBULENCE

by

Connor P. Mellett

December 2023

Thesis Advisor:	Jae Jun Kim
Co-Advisor:	Brij N. Agrawal

THIS PAGE INTENTIONALLY LEFT BLANK

REPORT DOCUMENTATION PAGE	*Form Approved OMB No. 0704-0188*

1. AGENCY USE ONLY ***(Leave blank)***	**2. REPORT DATE** December 2023	**3. REPORT TYPE AND DATES COVERED** Master’s thesis

4. TITLE AND SUBTITLE MULTI-CONJUGATE ADAPTIVE OPTICS PERFORMANCE IN SIMULATED ATMOSPHERIC DEEP TURBULENCE	**5. FUNDING NUMBERS**
6. AUTHOR(S) Connor P. Mellett	
7. PERFORMING ORGANIZATION NAME(S) AND ADDRESS(ES) Naval Postgraduate School Monterey, CA 93943-5000	**8. PERFORMING ORGANIZATION REPORT NUMBER**
9. SPONSORING / MONITORING AGENCY NAME(S) AND ADDRESS(ES) N/A	**10. SPONSORING / MONITORING AGENCY REPORT NUMBER**

11. SUPPLEMENTARY NOTES The views expressed in this thesis are those of the author and do not reflect the official policy or position of the Department of Defense or the U.S. Government.

12a. DISTRIBUTION / AVAILABILITY STATEMENT Approved for public release. Distribution is unlimited.	**12b. DISTRIBUTION CODE** A

13. ABSTRACT (maximum 200 words)

This research focuses on applying multi-conjugate adaptive optics to mitigate the adverse effects of atmospheric deep turbulence on a propagating laser beam. A unique multi-conjugate adaptive optics (MCAO) testbed was constructed and aligned to emulate and study the deep turbulence conditions characteristic of maritime environments. Experiments conducted on the testbed, using a low-power laser beam source, demonstrate that MCAO effectively improves the point spread function and reduces the wavefront error. By compensating wavefront aberrations at two conjugate planes along the beam path, turbulence-induced scintillation effects were also reduced. This research suggests that MCAO can potentially enhance the performance of high-energy laser systems, free-space optical laser communications, and ground-to-space imaging technologies by reducing the adverse effects of deep turbulence, such as beam spread and scintillation.

14. SUBJECT TERMS multi-conjugate adaptive optics, MCAO, deep turbulence, laser beam control, deformable mirror	**15. NUMBER OF PAGES** 73
	16. PRICE CODE

17. SECURITY CLASSIFICATION OF REPORT Unclassified	**18. SECURITY CLASSIFICATION OF THIS PAGE** Unclassified	**19. SECURITY CLASSIFICATION OF ABSTRACT** Unclassified	**20. LIMITATION OF ABSTRACT** UU

NSN 7540-01-280-5500

Standard Form 298 (Rev. 2-89)
Prescribed by ANSI Std. 239-18

THIS PAGE INTENTIONALLY LEFT BLANK

MULTI-CONJUGATE ADAPTIVE OPTICS PERFORMANCE IN SIMULATED ATMOSPHERIC DEEP TURBULENCE

Connor P. Mellett
Lieutenant, United States Navy
BS, United States Naval Academy, 2018

Submitted in partial fulfillment of the
requirements for the degree of

MASTER OF SCIENCE IN ASTRONAUTICAL ENGINEERING

from the

NAVAL POSTGRADUATE SCHOOL
December 2023

Approved by: Jae Jun Kim
Advisor

Brij N. Agrawal
Co-Advisor

Brian S. Bingham
Chair, Department of Mechanical and Aerospace Engineering

THIS PAGE INTENTIONALLY LEFT BLANK

ABSTRACT

This research focuses on applying multi-conjugate adaptive optics to mitigate the adverse effects of atmospheric deep turbulence on a propagating laser beam. A unique multi-conjugate adaptive optics (MCAO) testbed was constructed and aligned to emulate and study the deep turbulence conditions characteristic of maritime environments. Experiments conducted on the testbed, using a low-power laser beam source, demonstrate that MCAO effectively improves the point spread function and reduces the wavefront error. By compensating wavefront aberrations at two conjugate planes along the beam path, turbulence-induced scintillation effects were also reduced. This research suggests that MCAO can potentially enhance the performance of high-energy laser systems, free-space optical laser communications, and ground-to-space imaging technologies by reducing the adverse effects of deep turbulence, such as beam spread and scintillation.

THIS PAGE INTENTIONALLY LEFT BLANK

TABLE OF CONTENTS

LIST OF FIGURES

LIST OF TABLES

THIS PAGE INTENTIONALLY LEFT BLANK

LIST OF ACRONYMS AND ABBREVIATIONS

AO	adaptive optics
CCD	charge-coupled device
CMOS	complementary metal-oxide semiconductor
DM	deformable mirror
HEL	high-energy laser
MCAO	multi-conjugate adaptive optics
PIB	power in the bucket
PSF	point spread function

THIS PAGE INTENTIONALLY LEFT BLANK

ACKNOWLEDGMENTS

I would like to express my sincere gratitude to my advisor, Dr. Jae Jun Kim, and my co-advisor, Dr. Brij Agrawal, for their unwavering support and invaluable expertise in the field of optics. Their rich experience and the resources of the Adaptive Optics Center of Excellence labs were pivotal in steering this research to its conclusion.

I would also like to extend a special thank you to Dr. Ty Martinez from the Naval Research Laboratory. His decision to travel to the Naval Postgraduate School to assist with the alignment and final design of the MCAO testbed proved crucial. His profound knowledge and generosity in sharing it were instrumental in building a fully functional optical testbed, and for that, I am deeply appreciative.

I am also indebted to the entire Space Systems Academic Group at NPS. Being a part of this esteemed group has been both enlightening and enriching, revealing to me the expansive possibilities within the space industry.

Further, my acknowledgment would be incomplete without expressing my gratitude to the Naval Research Laboratory for its generous funding, which served as the backbone for this research.

Lastly, I want to convey my deepest gratitude to my friends and family. Their steadfast support has been an anchor during this pursuit, providing encouragement and grounding. Their belief in my potential, especially in moments of doubt, was invaluable.

THIS PAGE INTENTIONALLY LEFT BLANK

I. INTRODUCTION

The Navy’s interest in high-energy laser (HEL) systems as a defensive layer for ships has grown significantly in recent years. Similarly, military and commercial interest in optical communications links has grown as systems become more connected and the radio-frequency spectrum more contested. A significant challenge with these laser systems in maritime environments is deep atmospheric turbulence caused by the dynamic nature of air currents and densities, which affect the propagation of light waves. This turbulence adversely affects the propagating light waves in both amplitude and phase, ultimately diminishing the power delivered on targets. Drawing inspiration from the success of Multi-conjugate Adaptive Optics (MCAO) in ground-based telescopes, this research seeks to apply MCAO techniques to address optical challenges faced by laser and imaging systems operating under deep turbulence conditions.

As part of this research, a MCAO testbed is constructed and optically aligned, enabling the emulation of deep turbulence effects characteristic of the maritime horizontal beam propagation environment. Furthermore, this study experimentally utilizes the MCAO testbed to characterize the effects of deep turbulence and to test the performance of MCAO correction on a low-power laser beam. These experiments measure and compensate for wavefront distortions caused by deep turbulence effects by harnessing multiple sensors and two deformable mirrors.

The experimental results derived from the testbed indicate that MCAO holds promise in improving the point spread function and reducing the wavefront error of a beam through replicated deep turbulence conditions. Furthermore, the findings suggest a reduction in the scintillation of a propagating beam when employing MCAO. While our testbed research focuses on controlling a low-power laser beam, the implications and insights could potentially scale to larger HEL, optical laser communication, or ground-to-space imaging systems.

THIS PAGE INTENTIONALLY LEFT BLANK

II. BACKGROUND

This section examines atmospheric deep turbulence and its effects on optical signal propagation. It begins with an overview of atmospheric turbulence, its origins, and its challenges to optical systems. The focus then shifts to adaptive optics, highlighting classical single-mirror systems as well as advanced multi-conjugate adaptive optics.

A. ATMOSPHERIC DEEP TURBULENCE

This section provides background on atmospheric turbulence and its effects on optical signal propagation. Turbulence is caused by the variation in air densities, a product of atmospheric heating, cooling, and mixing processes. As light waves traverse these heterogeneous regions of air, they change direction slightly due to variations in the refractive index of the medium. This produces irradiance fluctuations, beam broadening, and loss of spatial coherence of the optical wavefront [1]. Turbulence effectively blurs an image captured through it, and it has been historically encountered in astronomy [2]. Figure 1 shows a simplified depiction of how atmospheric turbulence distorts a propagating optical wavefront, leading to blur at the receiving sensor.

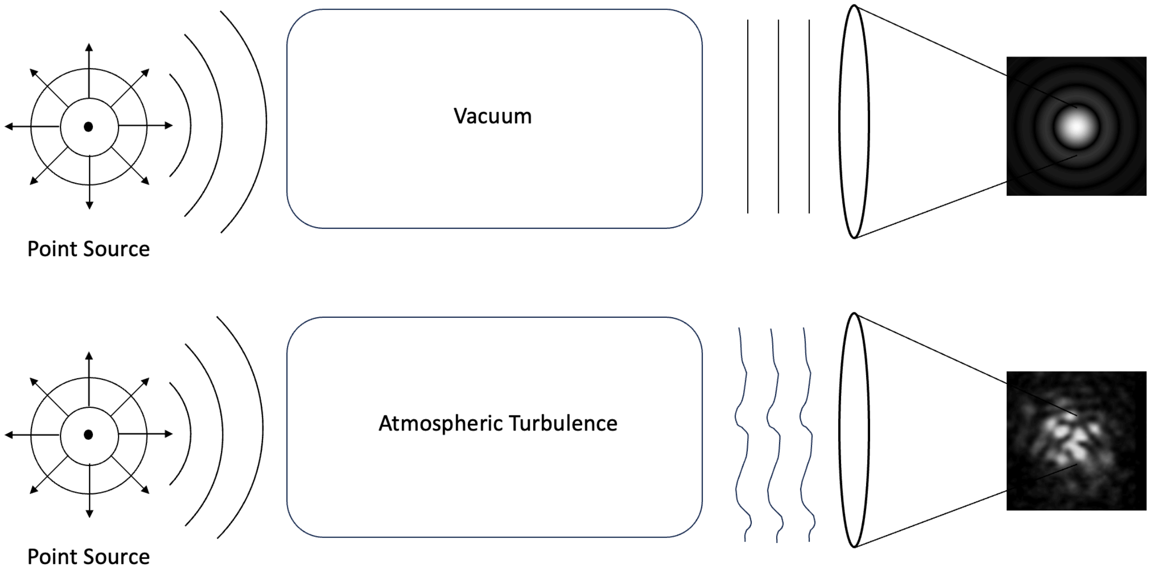

Figure 1. Atmospheric turbulence effects on propagation

A standard metric used to characterize the strength of atmospheric turbulence is the atmospheric coherence length, also known as Fried's parameter, denoted by r_0. Fried's parameter measures the spatial coherence across the line of sight and signifies the scale over which the air's refractive index appears uniform. Typically measured in centimeters, r_0 represents the maximum aperture size over which a telescope can achieve a diffraction-limited image. Any aperture larger than r_0 will not improve resolution performance [3].

Deep turbulence, sometimes called strong turbulence, is characteristic of horizontal propagation paths, particularly at low altitudes through a dense atmosphere. Deep turbulence contrasts with weaker atmospheric turbulence, often encountered in astronomy, where vertical propagation through a decreasingly dense atmosphere generally helps reduce the cumulative effects of turbulence. The horizontal path through deep turbulence significantly impacts the beam quality for HEL and free-space optical communication systems. Deep turbulence is characterized by a Rytov number, or log-amplitude variance, of $\sigma^2_X > 0.25$ [4].

A common negative optical effect of atmospheric turbulence, and one explored in this research, is called beam scintillation. Beam scintillation is defined as irradiance fluctuations within the cross-section of a beam [1]. Scintillation causes a reduction in signal-to-noise ratio and can induce deep random fades of an optical beam signal [1].

B. CLASSICAL ADAPTIVE OPTICS

The traditional approach to overcoming the effects of atmospheric turbulence has been single-mirror adaptive optics systems. In these systems, a distorted wavefront is reflected off the primary mirror of a telescope, also known as the pupil, and reimaged onto a downstream wavefront sensor. The wavefront sensor measures the incoming light's slopes to reconstruct the incoming wavefront's phase profile. This information can then be used in a closed-loop control system to command a deformable mirror (DM) shape to compensate for the phase variation across the distorted wavefront [2]. This way, optical performance can be improved towards the diffraction-limited image. An illustration of this concept, commonly applied to large aperture ground-based astrological telescopes, is shown in Figure 2. While classical, single-DM adaptive optics has proven helpful in correcting phase aberrations caused by weak atmospheric turbulence, it has difficulty in compensating deep atmospheric turbulence characterized by strong scintillation.

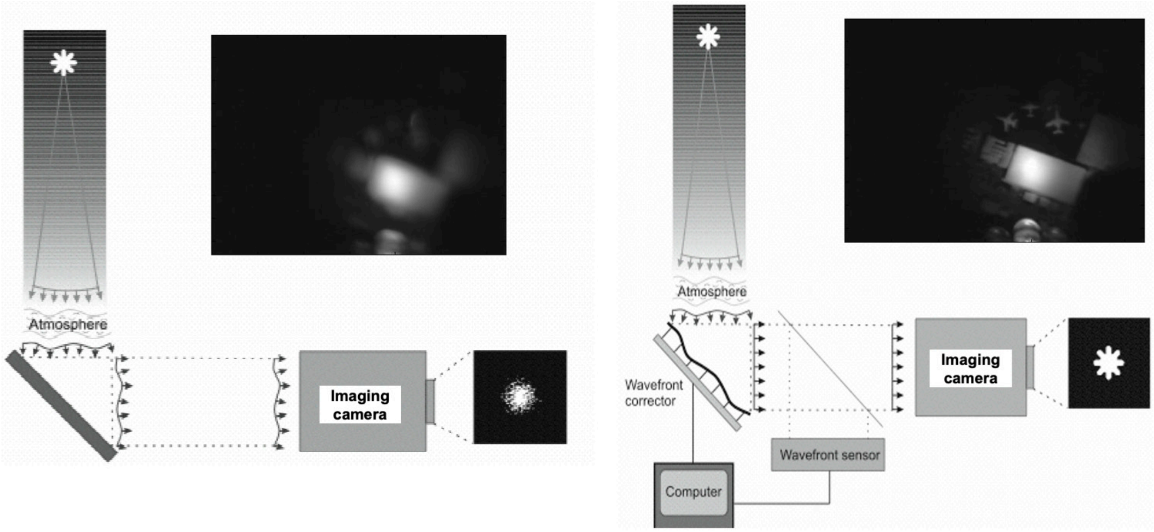

Without Adaptive Optics With Adaptive Optics

Figure 2. Compensation with classical adaptive optics. Source: [5]

C. MULTI-CONJUGATE ADAPTIVE OPTICS

The principle of multi-conjugate adaptive optics hinges on using two DMs, each aligned with different conjugate planes along the optical path, to correct for phase errors at their respective planes. Phase corrections made earlier in the propagation path contribute to reducing the scintillation effects. This capability contrasts with a single DM system, where the DM must be located at or near the pupil plane of the optical system. In this context, conjugation refers to the process where phase alterations introduced by one DM, followed by wavefront propagation, manifest as amplitude changes in the light [2]. Correction in multiple planes is achieved by reimaging the turbulent beam at multiple locations to separate wavefront sensors and DMs [6]. By correcting the phase at one plane and then propagating and correcting the phase again at another plane, the amplitude of the light wave, after it travels from the multi-conjugate DM to the pupil DM, matches the initially detected wavefront amplitude, thereby reducing the scintillation effects of deep turbulence [2]. Previous studies of MCAO performance have shown promising improvement in compensated point spread function (PSF) and Strehl ratio performance [2],[6], [7].

Figure 3 illustrates a simplified concept of using two DMs, each conjugate to a different plane in the beam propagation path. The entrance pupil plane, shown in red, represents the telescope aperture. The multi-conjugate plane represents some other plane along the beam's propagation path. The geometry of the follow-on optics determines the distance between planes. Conjugation is achieved by using reimaging optics, or relays, between the turbulence planes and the DMs, as well as between the DMs, to control the selection of the two planes [6].

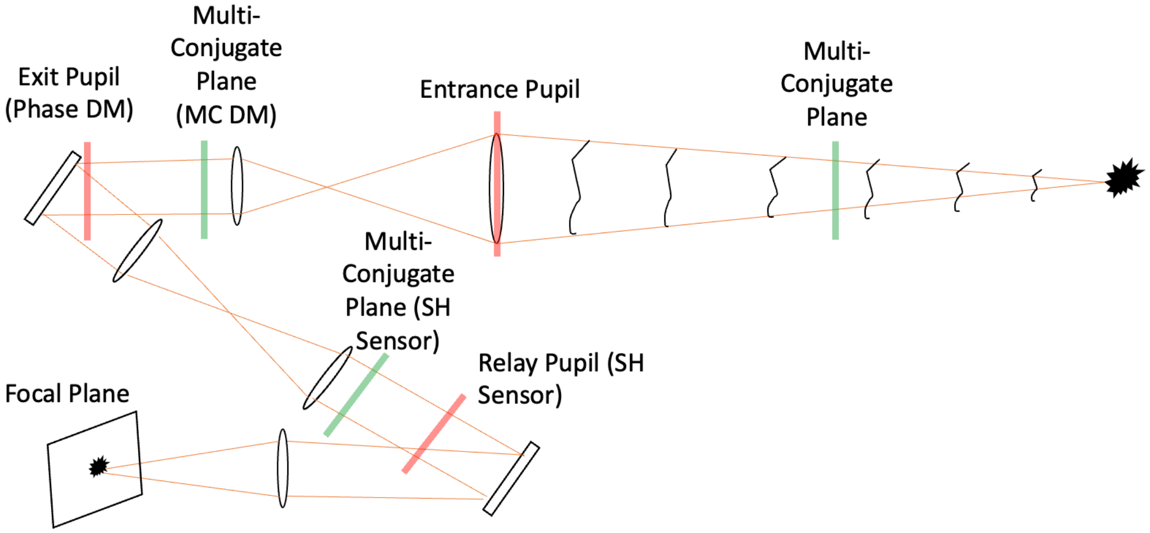

Figure 3. Multi-conjugate AO plane geometry. Source: [8]

III. METHODS

A. NPS ADAPTIVE OPTICS TESTBED OVERVIEW

This chapter describes the experimental setup of the NPS MCAO testbed. The testbed incorporates specialized components, including a Lumentum 1100 series helium-neon laser as the light source, Lexitek-produced turbulence phase plates for simulating atmospheric turbulence, and two deformable mirrors for wavefront correction. A series of CMOS monochrome industrial cameras are used for data acquisition. Interaction with and control of testbed components is orchestrated through several software suits operating on a high-performance Hewlett Packard workstation. This testbed enables advanced research and validation of MCAO systems under simulated but realistic atmospheric turbulence conditions. A photo of the MCAO testbed is shown in Figure 4.

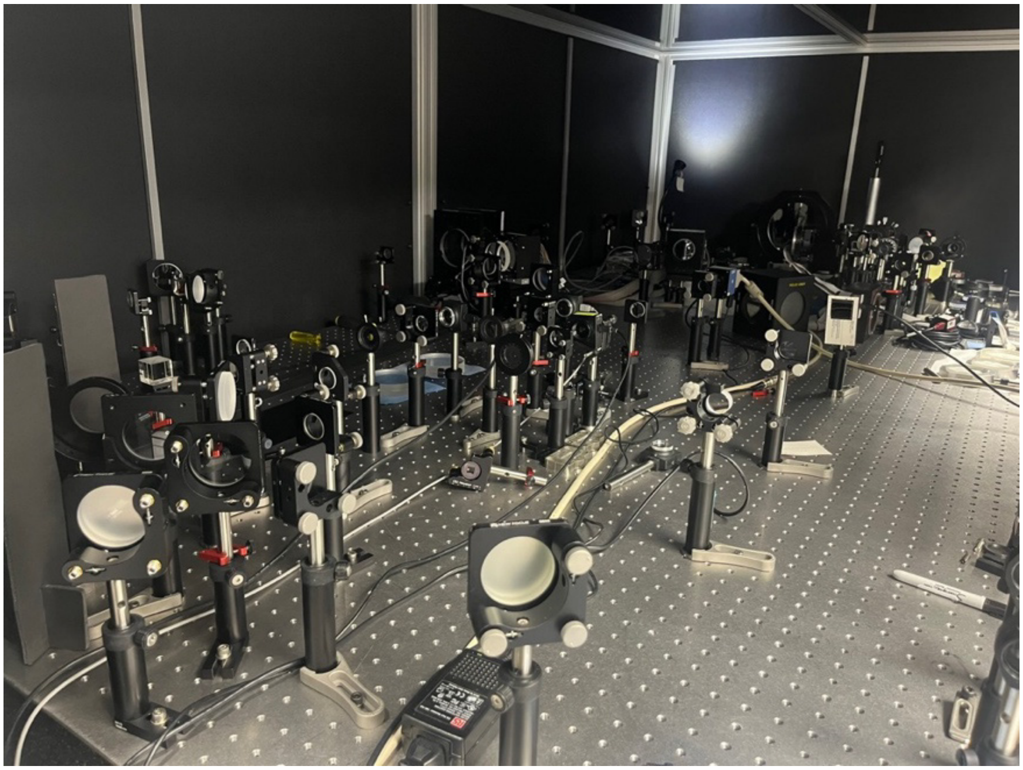

Figure 4. NPS MCAO testbed

Figure 5 shows the beam path of the laser in the MCAO testbed. The laser source is first passed through a microscopic optic and then an iris, helping achieve a point source of collimated light. The beam then passes sequentially through two phase plates, which simulate deep atmospheric turbulence by introducing pseudorandom phase aberrations. Following the phase plates, the laser is relayed to the two DMs: a 96-channel pupil DM and a 349-channel multi-conjugate DM, which corrects the wavefront distortions introduced by the turbulence. After reflecting off the DMs, the beam proceeds through a series of flat mirrors and beam splitters that guide the beam toward an array of sensors and cameras. These include pupil and PSF cameras and Shack-Hartmann wavefront sensors, facilitating data collection and feedback control to the two DMs.

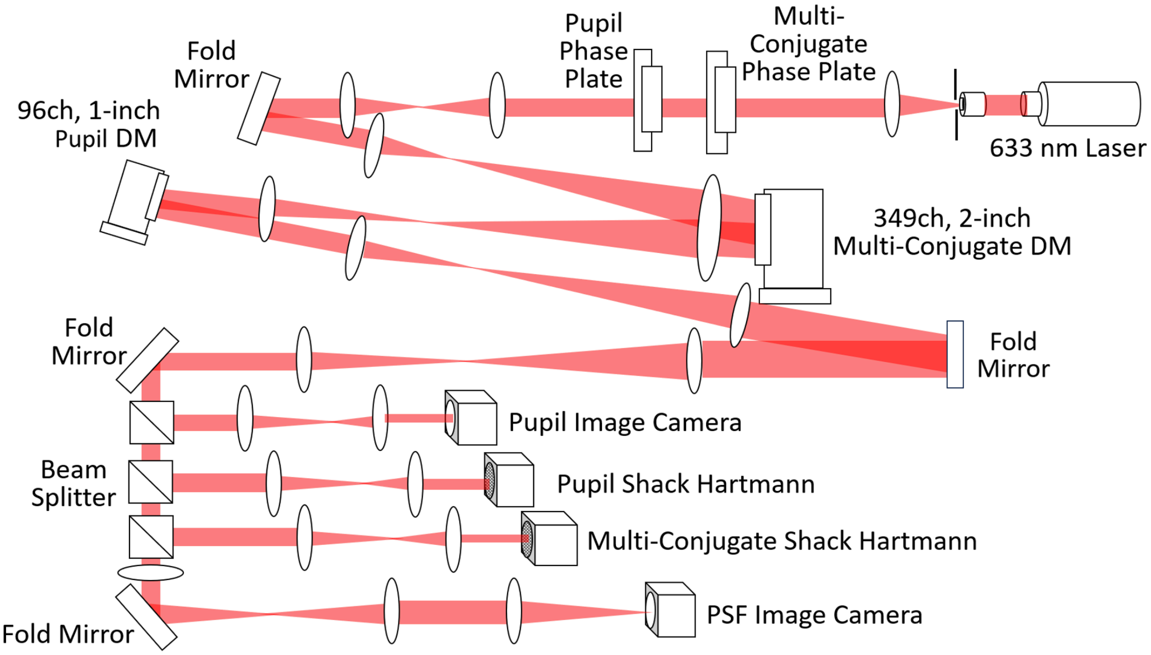

Figure 5. MCAO testbed optical path schematic

B. TESTBED COMPONENTS

1. Optical Table

The MCAO testbed is constructed atop a Kinetic Systems 5300 Series optical table, effectively isolating the optical path from vibration disturbances. The table is 120 inches (3048 mm) long, 59 inches (1499 mm) wide, and 18 inches (457 mm) thick. Mounting holes are 1/4-20 at 1-inch centers. The 5300 Series uses advanced dampers at its corners to provide high stability and reduce vibration disturbances [9]. The epoxy-bonded steel and honeycomb table offers high stability and rigidity, ensuring experimental repeatability. It sits in a temperature-controlled class 1000 clean room. A 5300 Series optical table is shown in Figure 6.

Figure 6. Kinetic Systems Inc. 5300 Series optical table. Source: [9].

2. Laser

The MCAO testbed uses a Lumentum 1100 series helium-neon laser as the beam source. The 1100 series features high power stability, low noise, and a long operating life [10]. This laser produces a 632.8 nm red laser with an output power of 1.5 mW. The visible wavelength and low power output are both helpful for alignment and testing as well as safe for the testbed's sensors and operators. For these reasons, it is an ideal laser source for aligning and testing the MCAO testbed. The 1100 series helium-neon laser is shown in Figure 7.

Figure 7. Lumentum 1100 series helium-neon laser. Source: [10].

3. Turbulence Phase Plates

This research utilized two Lexitek-produced turbulence phase plates to simulate the effects of atmospheric turbulence on beam propagation. Lexitek's turbulence phase plates offer a method of injecting well-characterized wavefront aberrations in the laboratory environment. The phase plates are built from a 100 mm diameter circular plate of precision-machined acrylic and cast optical polymer sandwiched between anti-reflective optical windows [11]. The plates are machined in a pseudorandom geometry to a specified r_0 value. This research uses plates designed to D/r_0 values of 15 and 25 to simulate varying degrees of atmospheric turbulence. An example of a Lexitek phase plate and its produced interferogram is shown in Figure 8.

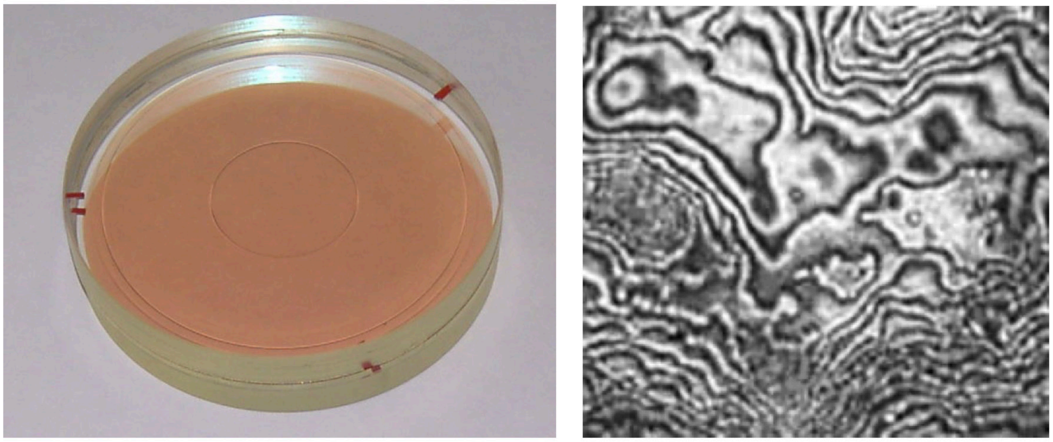

Figure 8. Lexitek Inc. turbulence phase plate and associated interferogram. Source: [11].

The phase plates are each mounted to a Lexitek HS-100 motorized rotary stage. The rotary stages hold the phase plates in place and provide a way to electronically control the rotation of the phase plate through a separate stepper motor control interface. The HS-100 incorporates a micro-stepping driver, which enables precise and repeatable rotary positioning [12]. It can be used in horizontal and vertical orientations and operate at speeds above 300 rpm [12]. This research mounts the rotary stages vertically to the optical bench and operates them at extremely low speeds of less than 1 rpm. The HS-100 motorized rotary stage is shown in Figure 9.

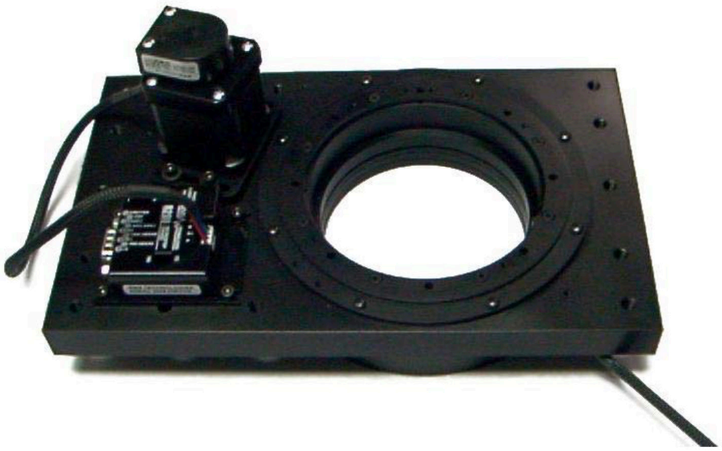

Figure 9. Lexitek Inc. HS-100 motorized rotary stage. Source: [12].

The motorized rotary stages are controlled through an Arcus Technology PMX-4EX-SA USB controller. This controller is an advanced 4-axis stepper standalone programmable motion controller [13]. On the MCAO testbed, it is configured to control two axes, X and Y, corresponding to the rotational movement of the HS-100 stages. The Arcus controller interfaces with the testbed host computer via a USB connection and is controlled through a dedicated Arcus GUI. The GUI enables precision control over the motors' range of motion, including speed, position, acceleration, and velocity profile. A PMX-4EX-SA is shown in Figure 10 with updated branding by Nippon Pulse.

Figure 10. PMX-4EX-SA 4-Axis stepper motion controller. Source: [13].

4. Deformable Mirrors

The first deformable mirror along the MCAO testbed optical path is a Flexible Optical 96-channel membrane deformable mirror. This DM is in a compact enclosure housing the mirror and its control electronics, including the power supply and digital-to-analog converter. It communicates with the testbed host computer through a single USB link. The mirror is a circular 1-inch (25.4 mm) clear aperture, continuous surface Aluminum-coated membrane, with 96 actuators [14]. The DM has an initial surface flatness of 150 nm peak-to-valley and provides a maximum deflection of 19 μm [14]. Given its relatively low-order surface figure control and relatively high actuator stroke, this research refers to the 96-channel DM as the pupil plane DM. The pupil plane DM is shown in Figure 11.

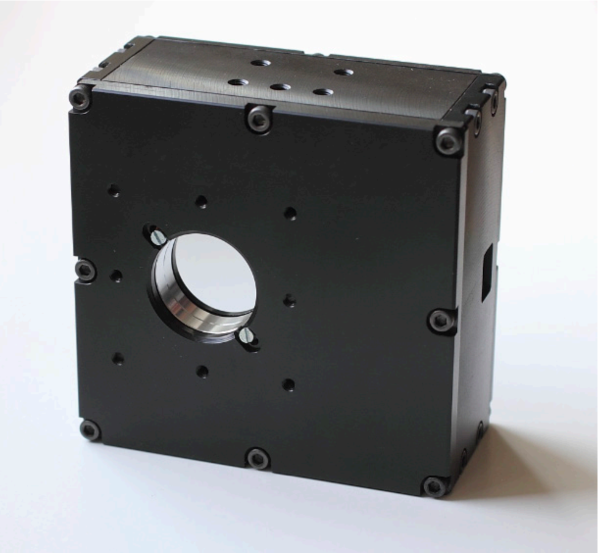

Figure 11. Flexible Optical 96-channel deformable mirror. Source: [14].

The second deformable mirror along the optical path is a Northrop Grumman Xinetics surface normal actuated (SNA) DM. The DM has a 53 mm circular clear aperture and 349 control channels utilizing lead magnesium niobate (PMN) electroceramic actuators, which exhibit little to no hysteresis, aging, or creep [15]. The actuators operate from 5–65 V and produce a maximum stroke of 2.5 μm. The control electronics and power amplifiers are contained within a separate enclosure that interfaces with the testbed host computer via serial connection. Given this DM's placement along the optical path at the multi-conjugate plane, this research refers to the Xinetics DM as the multi-conjugate plane DM. The multi-conjugate plane DM is shown in Figure 12.

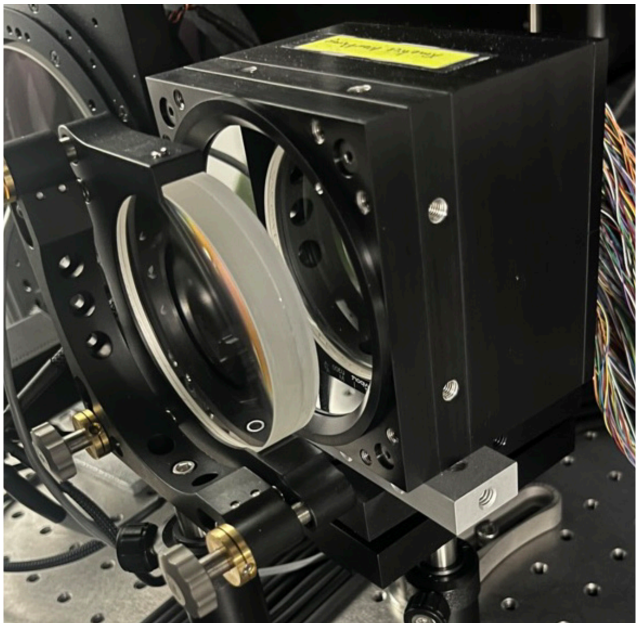

Figure 12. Northrop Grumman Xinetics 349-channel deformable mirror

5. Wavefront Sensors

The testbed uses two OKO Shack-Hartmann sensors to measure the beam wavefront shape. One is placed at the pupil plane and is used to close the control loop to the pupil DM, and one is placed at the multi-conjugate plane and is used to close the control loop to the multi-conjugate DM. Shack Hartman wavefronts sensors operate by placing a grid of microlenses in front of a CMOS sensor. The light passing through the microlens array is focused onto the sensor, forming a grid of spots: one per each illuminated microlens. When a distorted wavefront passes through the microlens array, the slope of the incoming light causes the spots to move slightly off the center of their grids. By measuring this spot movement, the slope of the wavefront can be calculated, and the shape of the incoming wavefront can be reconstructed. This operating principle is visualized in Figure 13.

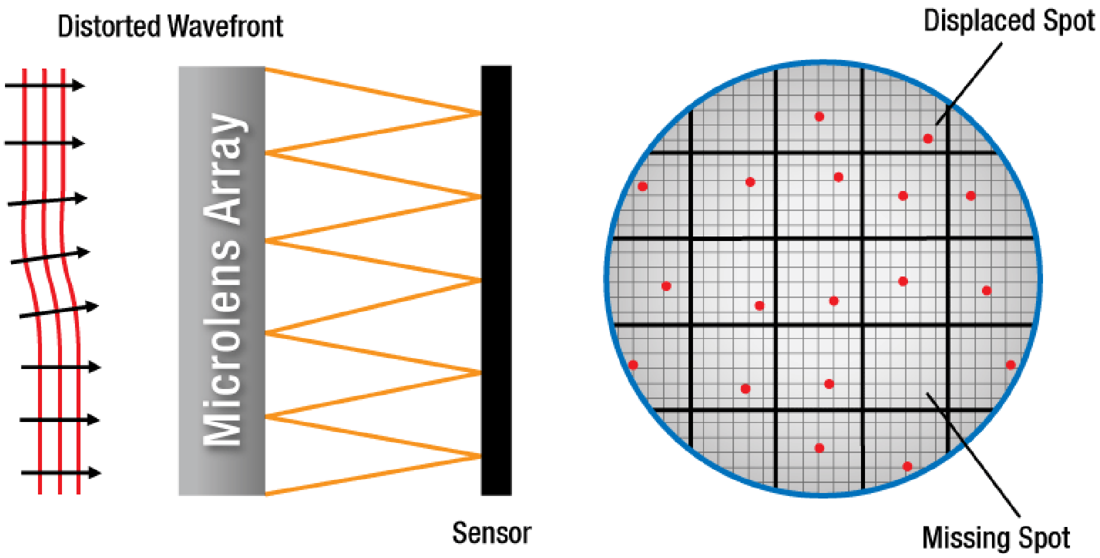

Figure 13. Shack-Hartman operating principle. Source: [16].

The pupil Shack-Hartmann comprises a hexagonal microlens array composed of 127 lenslets of 300 μm array pitch. The lenslets have a focal distance of 18 mm onto a 1280 x 1024 digital CCD array. The sensor interfaces with the testbed computer via a USB 2.0 connection [17].

The multi-conjugate Shack-Hartmann is comprised of an orthogonal array microlens array composed of 700 lenslets of 150 μm array pitch. The lenslets have a focal distance of 10 mm onto a 1280 x 1024 digital CMOS array. This sensor contains many more lenslets than the pupil sensor, which enables more precise measurement of the wavefront and helps to make more effective use of the 349 channels of the multi-conjugate DM. This sensor also interfaces with the testbed computer via a USB 2.0 connection [17].

6. Other Optical Components

The lenses used throughout the MCAO testbed are Edmund Optics 25 mm and 50 mm diameter MgF_2 coated achromatic lenses. The MgF_2 anti-reflective coating provides a very low reflectance value of less than 1.75% for wavelengths between 400 and 700 nm [18]. This is ideal for the 632 nm laser beam used on the MCAO testbed as it ensures minimal intensity loss along the optical path. Depending on the reimaging geometry, focal lengths vary between 200 mm and 500 mm.

Lenses are mounted to Newport adjustable optical lens mounts. These high-stability mounts provide precision pitch and yaw adjustment via three screws. These mounts sit atop Newport VPH series no-slip optical post holders, which provide stable vertical control of the optics and a pedestal base that ties it to the optical table.

7. Data Acquisition

The MCAO testbed incorporates two IDS UI-1540LE-M-GL CMOS monochrome industrial cameras for image acquisition: one each for the PSF image and the pupil plane image. These cameras have a 1280 x 1024 focal plane array with a 5.2 µm pixel pitch and 8-bit color depth [19]. Each camera interfaces with the testbed host computer through a USB connection. The cameras can be accessed and controlled through the IDS-provided software suite, uEye Cockpit. uEye enables users to preview and capture images as well as modify camera settings. A representative UI-1540LE-M-GL camera is shown in Figure 14.

Figure 14. IDS UI-1540E-M-GL industrial monochrome camera.
Source: [19].

8. Computer Interface and Software

Control and interaction with the MCAO testbed's DMs and sensors are through a single desktop computer workstation. The desktop computer is an HP Z8 G4 Workstation running Windows 10 on an Intel Xeon Silver 4216 processor. The Z8 is a robust desktop computer with 16 GB random access memory and a NVIDIA Quadro T1000 Graphics card. The high performance of this computer enables simultaneous control and communication with the two DMs, four imagers, and two rotary stages necessary to run the MCAO testbed. This research used four main software tools to run the MCAO testbed.

The Woofer DM is controlled by OKO's FrontSurfer software, which is provided with its 96-channel MMDM. It contains the comprehensive toolset necessary to ingest Shack Hartmann wavefront sensor data, apply open and closed loop DM control commands, and measure wavefront error at the pupil plane. Proper camera settings and feedback control parameters were integral in closing the control loop for the woofer DM. The comprehensive set of FrontSurfer parameters used for this research can be found in Appendix B.

The multi-conjugate DM is controlled by a custom MATLAB script, which can be found in Appendix C. This script manages the connection with the control electronics for the multi-conjugate DM, ingests image data from the multi-conjugate plane Shack Hartmann wavefront sensor, and performs the algorithm to close the feedback control loop with the DM.

Images from the PSF and pupil cameras are captured using the IDS uEye Cockpit software suite. This research requires consistent camera settings across the captured images to enable accurate post-processing. The comprehensive set of uEye parameters used in this experiment is found in Appendix B.

The Arcus PMS-4EX-SA GUI controls the motorized rotary stages for the phase plate. This software establishes the USB connection with the stepper motion controller and offers a variety of control options for the stages. This research chose several random target locations around the phase plates and drove the rotary stages to those positions to take measurements across various simulated turbulence conditions.

C. CALIBRATION AND ALIGNMENT

Proper calibration and alignment of the MCAO testbed is essential to its functionality and is often a significant challenge when working with sensitive optical systems. There is always a need to ensure acceptable beam quality, performance, and stability. This is accomplished through careful placement of the optical components and meticulous use of shear plates and irises. A carefully planned and systematic approach to aligning the components, starting at the laser source and concluding at the PSF camera, ensured that the testbed's beam path was stable and that the turbulence-free reference beam was of sufficient quality. In this way, unintended beam aberrations from testbed components were minimized.

Calibration and alignment of the MCAO testbed proved particularly challenging since it measures and corrects wavefronts on two different planes. This necessitated multiple pairs of relay lenses to place the pupil camera, pupil wavefront sensor, and pupil DM at the relayed pupil turbulence plane. This also applied to the multi-conjugate wavefront sensor and DM.

Calibration of the sensors is a critical step to ensure accurate measurement and correction of wavefront distortions. This process begins with establishing a calibration baseline by capturing the behavior of a known, turbulence-free reference beam. Setting the DMs to their flat settings, we direct the reference beam through the system, enabling the sensors to capture a reference wavefront. This reference is crucial as it serves as a benchmark against which the performance of the AO experiments can be assessed.

D. EXPERIMENTAL APPROACH

1. Experiment Design

The experimental design was structured to evaluate both pupil AO and MCAO under varying intensities of static deep turbulence. Detailed breakdowns of the experimental setups are shown in Appendix A. First, the turbulence-free beam was characterized, and the effects of both pupil AO and MCAO were measured to verify controllability and establish a benchmark against which the turbulent beam measurements could be compared. Then, the AO control was evaluated against three overarching turbulence levels, scaled in severity. The least severe condition utilized a phase plate of D/r_0 equal to 15 at the multi-conjugate plane, followed by a moderate condition with a D/r_0 equal to 25. The most severe condition combined a phase plate with a D/r_0 equal to 15 at the pupil plane and a D/r_0 equal to 25 at the multi-conjugate plane. In order to incorporate statistical variability, each level of turbulence was tested at five randomly chosen phase plate locations, introducing slight variations and enriching the dataset for better trend analysis.

Measurements were conducted sequentially for each simulated turbulence condition. Initially, the DMs were set to their flat state to capture the uncompensated beam measurements. This was followed by the activation of pupil AO to assess classical control. Finally, the multi-conjugate DM was engaged concurrently with the pupil DM to evaluate the cumulative effect of dual DM use in a MCAO configuration. This progressive experimental approach is captured in detail in Appendix A.

2. Beam Quality Metrics

This experiment concentrated on three primary metrics to assess beam quality. The first metric, the point spread function (PSF), characterizes the beam spread pattern, indicating how the beam would appear at its destination, landing on a target or received by a sensor. Specifically, the peak intensity within the PSF provides a quantitative measure of the beam's focus and quality.

The second metric examined is the pupil wavefront error, which quantifies the divergence of the actual beam wavefront from the ideal flat wavefront expected in turbulence-free propagation. The wavefront error helps predict beam spread and scintillation, affecting beam power transmission efficiency. The DMs in the testbed aim to correct this error, thereby enhancing beam quality as reflected in the quantitative wavefront measures of peak-to-valley distance and root mean squared (RMS) error.

The third and final metric is scintillation, or intensity log-amplitude variance, observed within the beam. Scintillation is the manifestation of the interference patterns, both constructive and destructive, throughout the beam. It can be observed by capturing images of the pupil plane. This experiment evaluates the power within the beam's cross-sectional area, known as power in the bucket (PIB), and the intensity log-amplitude variance to provide insights into the qualitative aspects of beam propagation. The specific data points related to these metrics are detailed in Appendix A, Table 1.

3. Feedback Control Process

The MCAO testbed, as configured, uses two separate processes to control the two DMs. The pupil DM is controlled through OKO's FrontSurfer software. In contrast, the multi-conjugate DM is controlled through a custom MATLAB script, which is provided in Appendix C. While each DM is controlled via a separate interface, the feedback control process is similar for both. The wavefronts at the associated planes are measured by the Shack-Hartmann sensors. Then, poke basis modal control is applied to the mirrors to minimize wavefront RMS error. The MCAO tested is incapable of real-time correction for dynamic deep turbulence. For this research, the MCAO control process is accomplished iteratively.

As discussed in this section, first pupil AO and then MCAO are tested against each simulated turbulence condition. After taking uncompensated measurements for the turbulence condition, FrontSurfer initiates the pupil DM's control loop. This control loop is run until the RMS error plateaus at some minimum value. The loop generally takes on the order of several seconds to reach an RMS plateau. Then, the control loop is paused, freezing the pupil DM shape. Measurements are taken at this stage, representing the classical pupil AO case.

Then, the MCAO control loop is applied using the MATLAB script in Appendix C. This loop runs for a preset number of iterations, in this case 30 times, to allow the MCAO DM to minimize RMS error. Generally, the minimum RMS error was reached in approximately ten iterations. After the MCAO control loop, the mirror control values are again frozen, and a final set of measurements is taken, representing the MCAO case.

4. Data Collection and Processing

Data collection for this experiment was accomplished by capturing three grayscale images and one screenshot of the FrontSurfer software for each tested turbulence and compensation scenario. The images were later used for post-experiment processing to calculate the beam quality metrics. It was vital to hold the sensor settings constant throughout data acquisition to ensure accurate post-processing and analysis. The chosen sensor settings are found in Appendix B.

The first data point, the PSF image, was captured using the uEye software. The second data point, the pupil image, was also captured using the uEye software. The third data point, the multi-conjugate wavefront sensor image, was captured automatically by saving the MATLAB workspace data following the conclusion of the MCAO control loop. The final data point was a screenshot of the measured wavefront displayed by the FrontSurfer software.

MATLAB was used to analyze the captured images and extract pertinent measurements from the raw images, such as peak intensity or intensity variation, where necessary. A complete listing of the calculated and measured data can be found in Appendix A, Table 2.

THIS PAGE INTENTIONALLY LEFT BLANK

IV. ANALYSIS

This chapter presents and analyzes results from the MCAO testbed deep turbulence compensation experiment. First, the effects of the turbulence phase plates are characterized both in their effect on the PSF as well as their effect on the pupil plane image. Second, the performance of pupil AO and MCAO on PSF compensation is analyzed. Third, the performance of pupil AO and MCAO on wavefront propagation is analyzed. Finally, the effects of pupil AO and MCAO on pupil plane intensity are analyzed.

A. SIMULATED DEEP TURBULENCE EFFECTS

Figure 15 clearly illustrates the impact of phase plate insertions on the beam's quality. Each PSF image was taken with the DMs in their nominal flat state. The turbulence-free beam, evident in its relative sharpness, contrasts markedly with the other three images that show distinct aberrations due to phase plate configurations. These aberrations result in a noticeable beam spread, decreasing peak intensity as captured by the PSF camera. In practical applications, such deep turbulence effects would reduce the target's beam intensity, highlighting the need for AO-enabled improvements. As expected, beam spread increases from the milder phase plate configuration, $D/r_0 = 15$ at the multi-conjugate plane, to the most severe combination, $D/r_0 = 15$ at the pupil plane and $D/r_0 = 25$ at the multi-conjugate plane. Although Figure 15 presents a single PSF frame for each turbulence level, the rotary stages enable a broad range of PSF variations due to their pseudorandom construction.

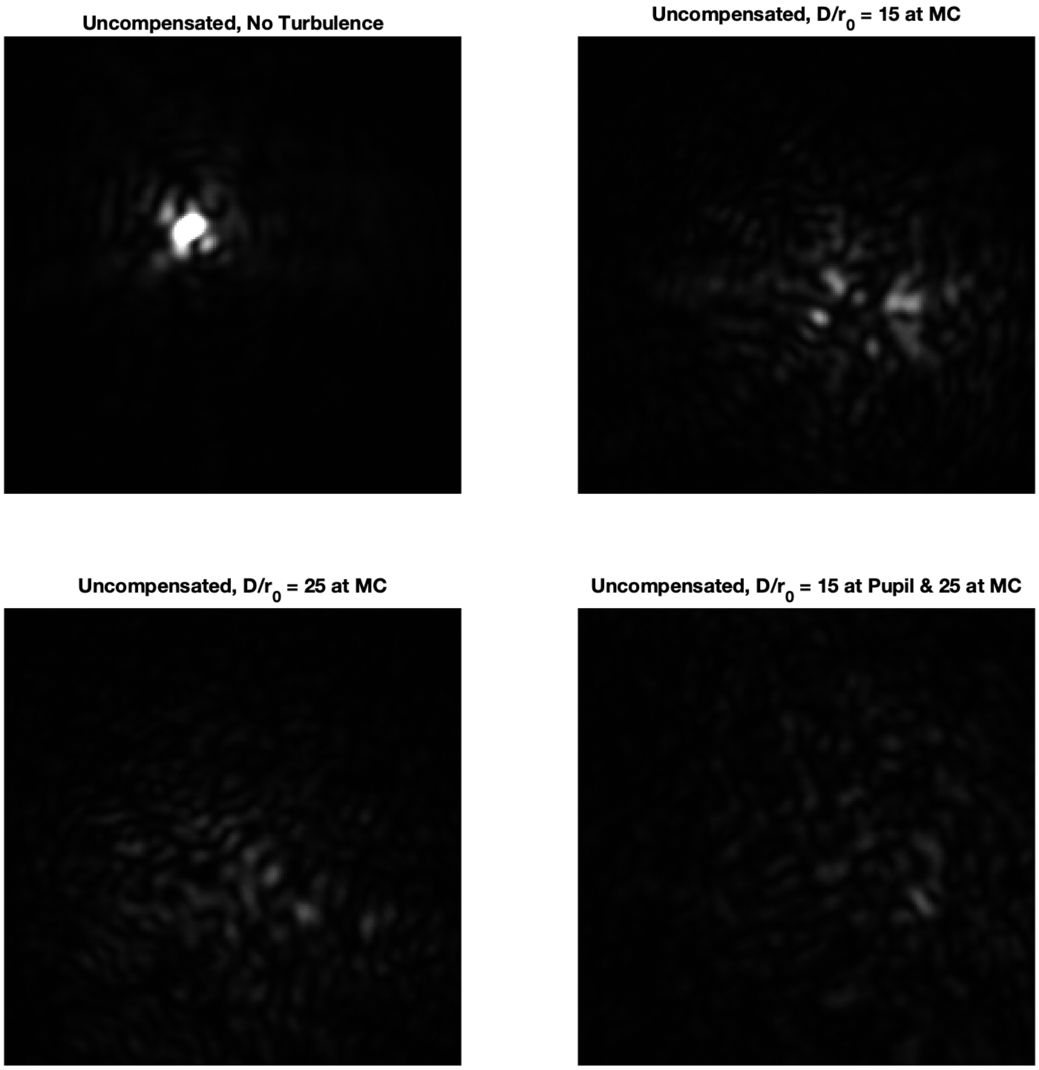

Figure 15. Example deep turbulence effects on measured PSF

Figure 16 similarly shows the impact of the simulated deep turbulence on the beam quality. In this case, the camera captures the image at the pupil plane or where the beam effectively enters the aperture. In an ideal system, the pupil image would be a perfect circle of uniform intensity representing the beam's coherence along its propagation path. As evident in the turbulence-free pupil image, the MCAO testbed's pupil image is not uniform in intensity and suffers fading around the edges. It does, however, appear relatively uniform in intensity towards the center of the beam. Comparatively, the aberrated beams display pronounced intensity fluctuations across the wavefront, as evident from the granular appearance of the pupil images. Such intensity peaks and troughs stem from constructive and destructive interference along the propagating wavefront, an effect known as scintillation and quantified by the Rytov variation parameter. It is important to note that some of this aberration is due to manufacturing artifacts in the phase wheel construction, as evidenced by the arc patterns in Figure 16.

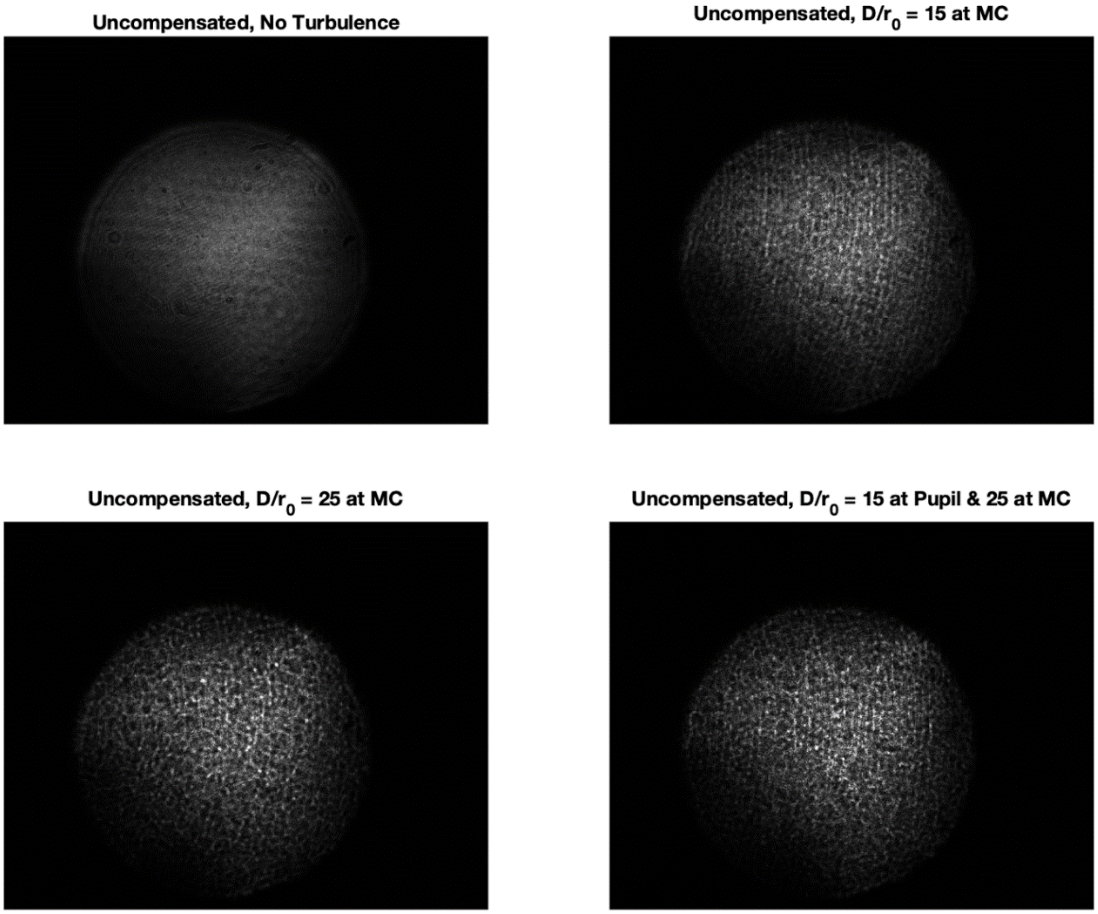
Uncompensated, No Turbulence

Uncompensated, $D/r_0 = 15$ at MC

Uncompensated, $D/r_0 = 25$ at MC

Uncompensated, $D/r_0 = 15$ at Pupil & 25 at MC

Figure 16. Examples of deep turbulence effects on measured pupil plane image

B. PSF ANALYSIS

This section presents several examples of PSF compensation across the three turbulence conditions and the three compensation levels. It examines captured PSF images from the MCAO testbed and screenshots from the FrontSurfer program, which calculates an estimated PSF based on wavefront measurements obtained by the pupil Shack-Hartmann sensor. Finally, it presents graphs of the complete experimental data, which show that MCAO provides a significant PSF performance increase over conventional pupil AO.

Figure 17 shows one example of AO compensation progression for a turbulence simulation run using the phase plate equivalent to $D/r_0 = 15$ at the multi-conjugate plane. As the captured PSFs display, beam spread is reduced, and the maximum intensity is increased using Pupil AO and MCAO. MCAO visibly produces a marked improvement over Pupil AO alone. This PSF progression is one of five datasets captured at this turbulence level. The other datasets rotate the phase plates to propagate the beam through different locations on the plate, resulting in slightly different beam aberrations.

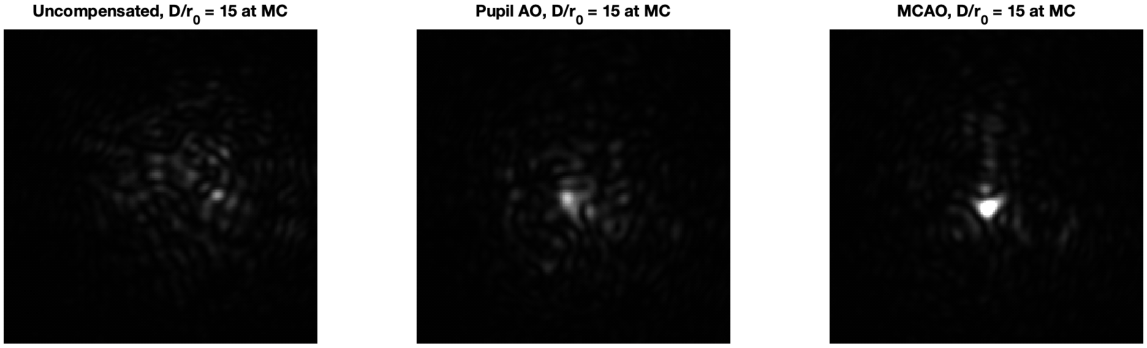

Figure 17. PSF compensation progression, mild case

Figure 18 displays the FrontSurfer PSF estimations based on pupil Shack-Hartmann measurements. Visibly, the estimated PSF progression in Figure 18 corresponds relatively closely with the actual PSF images captured in Figure 17. In situ, this confirmed that the pupil Shack-Hartmann was correctly measuring the wavefront and successfully closing the pupil AO feedback loop.

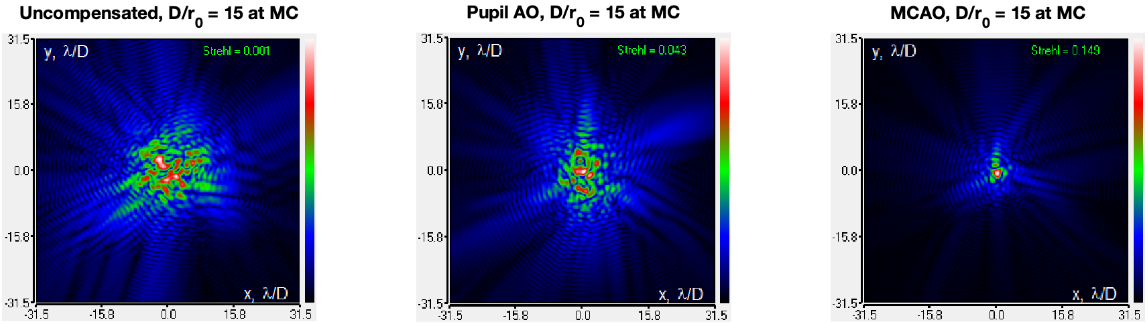
Uncompensated, D/r_0 = 15 at MC

Pupil AO, D/r_0 = 15 at MC

MCAO, D/r_0 = 15 at MC

Figure 18. Shack-Hartmann estimated PSF compensation progression, mild case

Figure 19 shows another example of the MCAO correction progression. This case is for a more severe turbulence case and uses the phase plate equivalent to $D/r_0 = 25$ at the multi-conjugate plane. The uncompensated PSF clearly shows an initially significant beam spread. Pupil AO alone reduces beam spread to a degree, but it is not until the multi-conjugate DM loop is also closed that significant intensity improvement can be seen. The estimated PSFs in Figure 20 closely correlate with the measured PSFs.

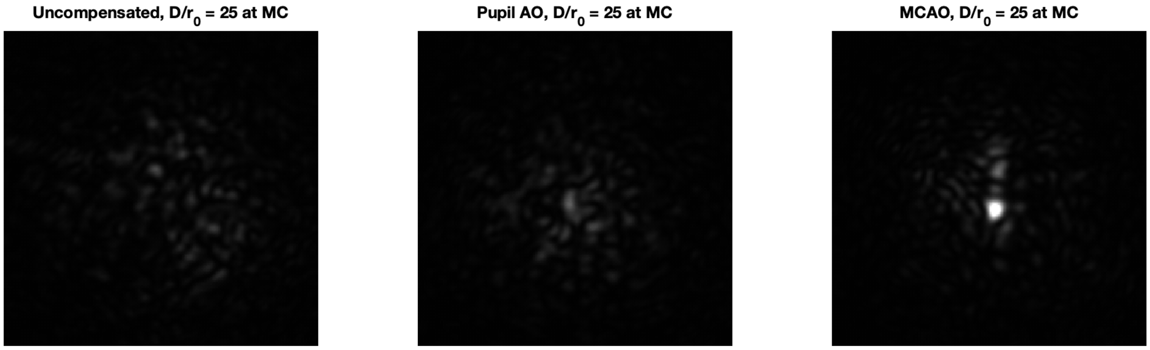
Uncompensated, D/r_0 = 25 at MC

Pupil AO, D/r_0 = 25 at MC

MCAO, D/r_0 = 25 at MC

Figure 19. PSF compensation progression, moderate case

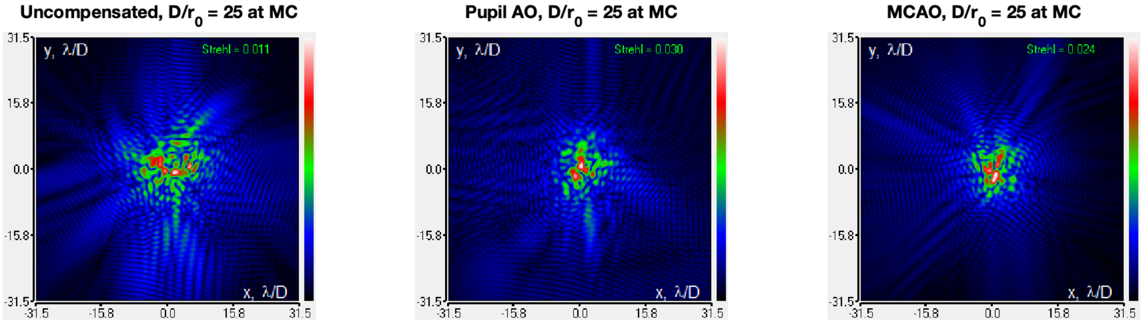

Figure 20. Shack-Hartmann estimated PSF compensation progression, moderate case

Figure 21 presents the PSF compensation under the harshest deep turbulence simulated in this experiment. This uses the phase plate with equivalences of $D/r_0 = 15$ at the pupil plane and $D/r_0 = 25$ at the multi-conjugate plane. Uncompensated, the PSF experiences significant beam spreading, and its peak intensity decreases markedly. Under such high turbulence, the PSF is often barely visible in the uEye Cockpit software. Although Pupil AO and MCAO improve the PSF quality, their effectiveness is limited compared to milder turbulence scenarios in this section.

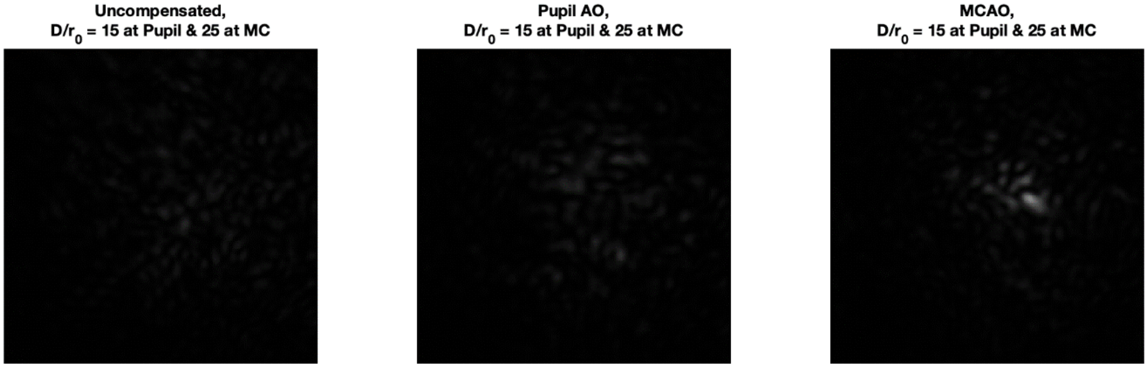

Figure 21. PSF compensation progression, severe case

In Figure 22, the PSFs estimated from pupil Shack-Hartmann measurements diverge from those captured in Figure 21. While the less turbulent cases previously discussed showed close agreement between estimated and captured PSFs, this severe turbulence challenges the pupil Shack-Hartmann sensor capabilities. The substantial phase and intensity fluctuations at this turbulence level hinder the Shack-Hartmann wavefront sensor's ability to generate accurate centroid measurements and wavefront slope estimates. Absent consistent and precise slope data, feedback control for the pupil DM becomes significantly less effective, as demonstrated.

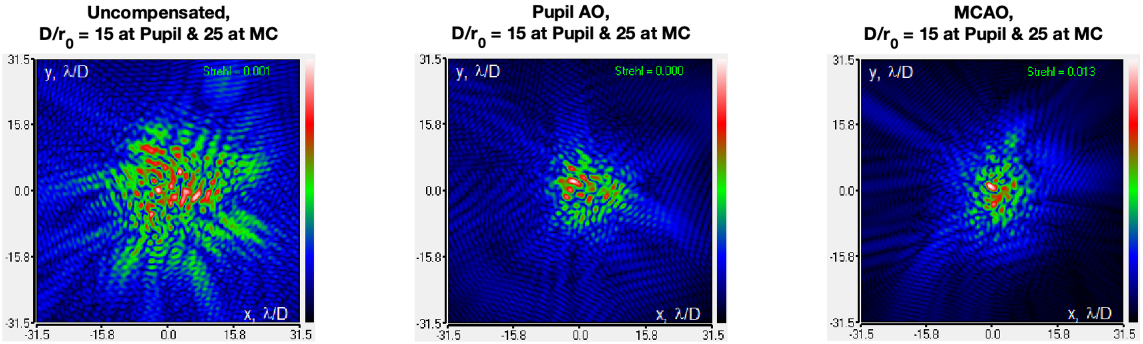

Figure 22. Shack-Hartmann estimated PSF compensation progression, severe case

Figure 23 graphs the PSF peak intensity measured under each turbulence condition and compensation method we tested. As the turbulence conditions become more severe, there is a pronounced reduction in uncompensated peak intensity. The application of Pupil AO and MCAO methods offers notable improvements in PSF intensity in nearly all test cases, reaching the camera pixel saturation value of 255 in several cases.

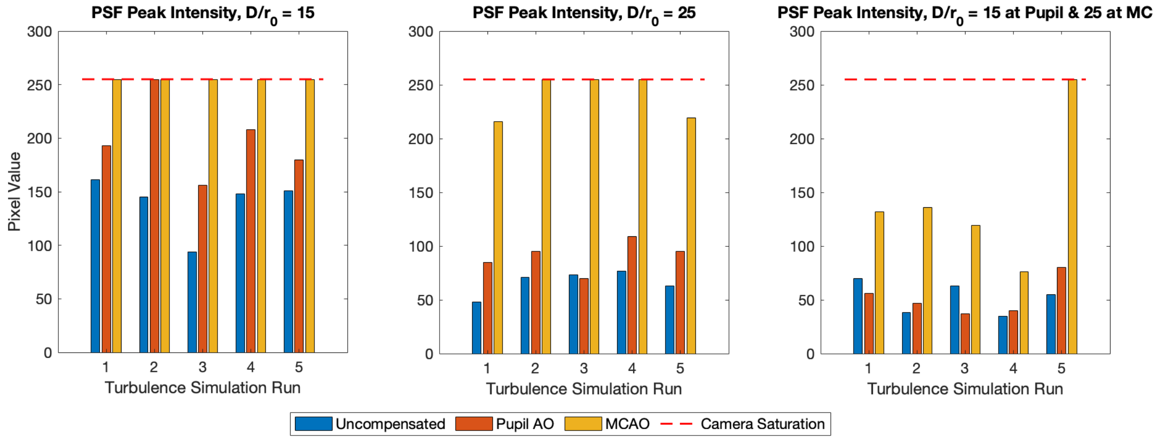

Figure 23. Measured peak PSF pixel intensities

Figure 24 displays the mean PSF peak intensity value across the five pseudorandom turbulence simulations at each turbulence level and compensation technique. The graphs show that MCAO significantly improved peak intensity under the three turbulence levels. Pupil AO produced moderate improvement at the milder turbulence levels. However, Pupil AO alone does not consistently improve PSF peak intensity in the severe case. This diminished performance can be attributed to the difficulties associated with accurately measuring the wavefront slopes at the pupil and the challenges of consistently closing the feedback control loop amidst intense, deep turbulence.

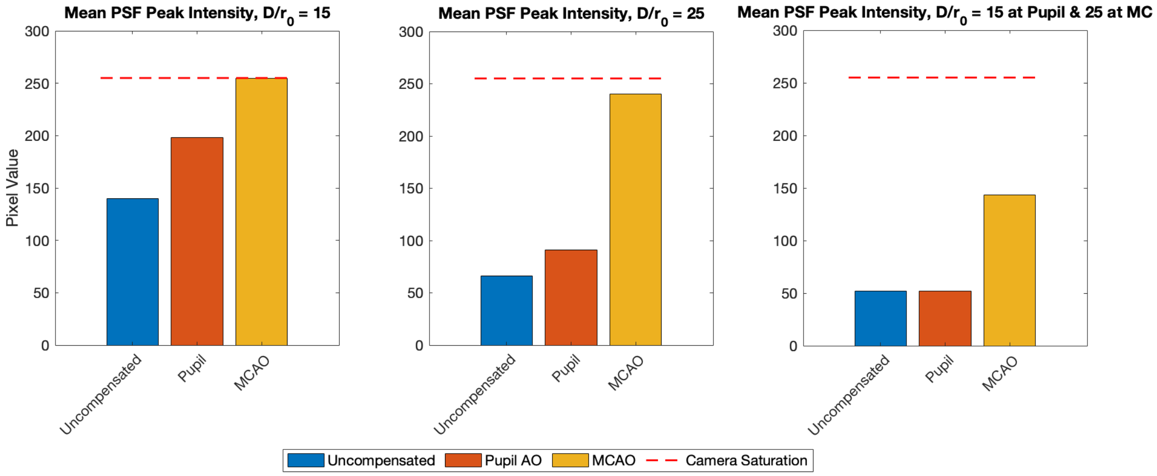

Figure 24. Mean peak PSF pixel intensities

C. PUPIL WAVEFRONT ERROR ANALYSIS

This section analyzes the effects of pupil AO and MCAO on the wavefront error measured at the pupil plane. It presents an example of pupil wavefront compensation using the two AO techniques. The effectiveness of this compensation is quantified, in part, by the wavefront peak-to-valley, which highlights the maximum and minimum extremes of the incoming wavefront distortions. Additionally, the wavefront root-mean-square (RMS) error is used to characterize the standard deviation of aberration across the wavefront, providing a comprehensive measure of its overall variation.

Figure 25 shows a screenshot of the FrontSurfer Shack-Hartmann grid. This feature of the FrontSurfer software captures images from the pupil Shack-Hartmann sensor and, using a reference grid, calculates the slopes of the incoming wavefront. From the slopes, the software can reconstruct the shape of the incoming wavefront for both measurement and feedback control to the pupil DM.

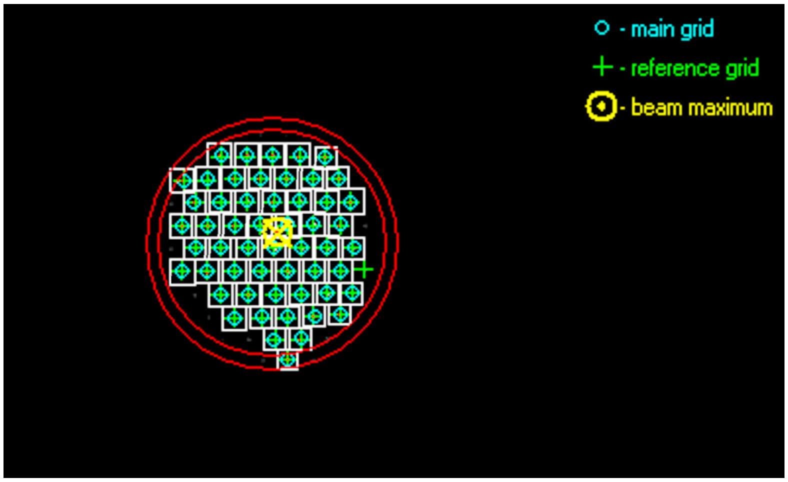

Figure 25. FrontSurfer Shack-Hartmann wavefront sensor and centroid visualization

Figure 26 shows an example of AO compensation progression for a turbulence simulation run using the phase plate equivalent to D/r₀ = 15 at the multi-conjugate plane. As the captured interferograms show, wavefront distortion is reduced using Pupil AO and MCAO. MCAO visibly produces a much flatter wavefront over Pupil AO alone. A low wavefront error is important for laser beam propagation as it shows minimal deviations from the ideal, flat wavefront shape. This ensures increased beam intensity and less wavefront distortion, leading to efficient energy transmission and reduced beam spread.

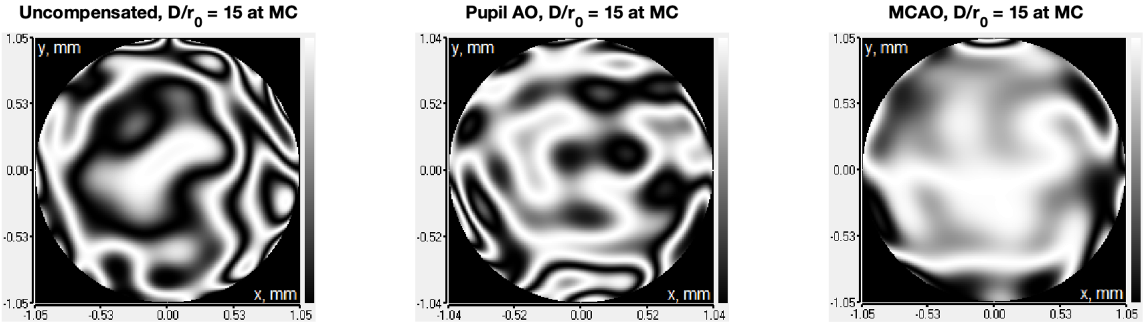

Figure 26. Shack-Hartmann estimated interferogram compensation progression, mild case

Figure 27 graphs the wavefront peak-to-valley measured under each turbulence condition and compensation method tested. As the turbulence conditions become more severe, there is a pronounced increase in uncompensated peak-to-valley error. Looking across the various turbulence simulation cases, it is unclear whether pupil AO and MCAO drive down the peak-to-valley error.

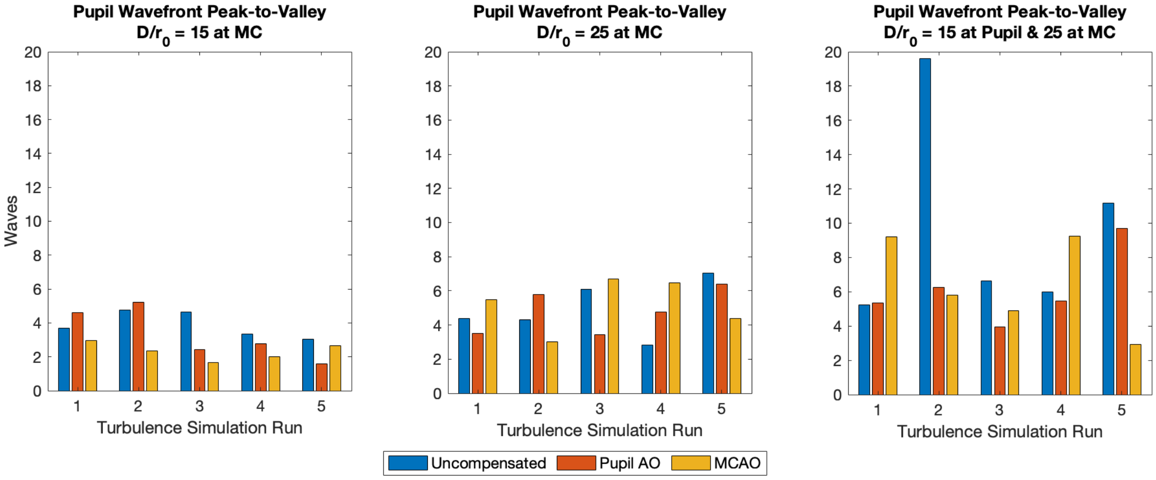

Figure 27. Measured pupil wavefront peak-to-valley

Wavefront measurements indicated that prominent peaks and valleys in the measured wavefront tended to congregate along the periphery of the beam. For example, this is evidenced in the dense fringes towards the outside of the apertures seen in Figure 26. There are two reasons why pupil AO and MCAO do not consistently drive peak-to-valley lower in most cases. First, the actuators on the periphery of the DMs might be limited in their ability to compensate for significant phase errors located near the edges of the continuous face sheet DM. Second, the spots produced by the Shack-Hartmann lenslets are generally dimmer along the periphery of the beam due to less light diffracting through those outer lenslets. This can cause unreliable centroid calculation and, thus, poor slope measurements at these areas of the beam. This sensor limitation can sometimes measure an artificially high peak-to-valley error, which may be reflected in these results.

Figure 28 displays the mean pupil wavefront peak-to-valley error across the five pseudorandom turbulence simulations at each turbulence level and compensation technique. These graphs indicate that pupil and MCAO tended to reduce wavefront peak-to-valley error on average. This trend was not immediately evident in Figure 27 but suggests there is general improvement by this measure.

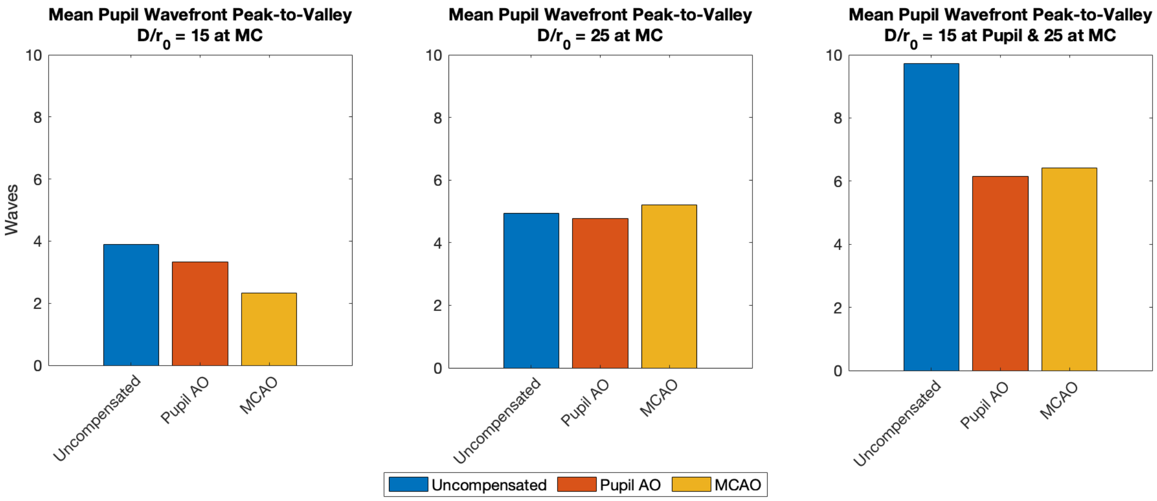

Figure 28. Mean pupil wavefront peak-to-valley

A better measure of AO compensation is wavefront RMS error because it captures the deviation across the wavefront on average rather than just at the extremes. Figure 29 shows the wavefront RMS error measured under each turbulence condition and compensation method tested. As the turbulence conditions become more severe, there is a marked increase in uncompensated RMS error. Across the simulated turbulence cases, pupil AO and MCAO both show a clear improvement in RMS error. This translates to reduced beam spread and improved PSF peak intensity, as highlighted earlier in this chapter.

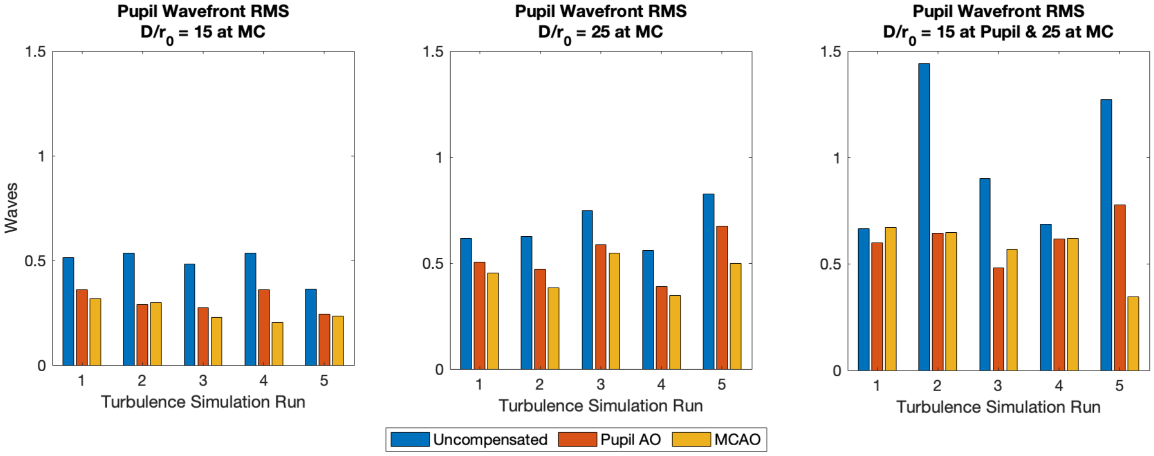

Figure 29. Measured pupil wavefront root mean squared error

Figure 30 depicts the mean pupil RMS wavefront error across the five pseudorandom turbulence simulations for each turbulence level and compensation technique. The graphs demonstrate that the RMS error is reduced across all turbulence levels. Furthermore, MCAO consistently provides a more significant improvement compared to pupil AO. This trend is anticipated as the DMs' control loops were designed to minimize the RMS measurement. The observed trend in RMS error aligns well with the PSF peak intensity measurements previously discussed in this chapter.

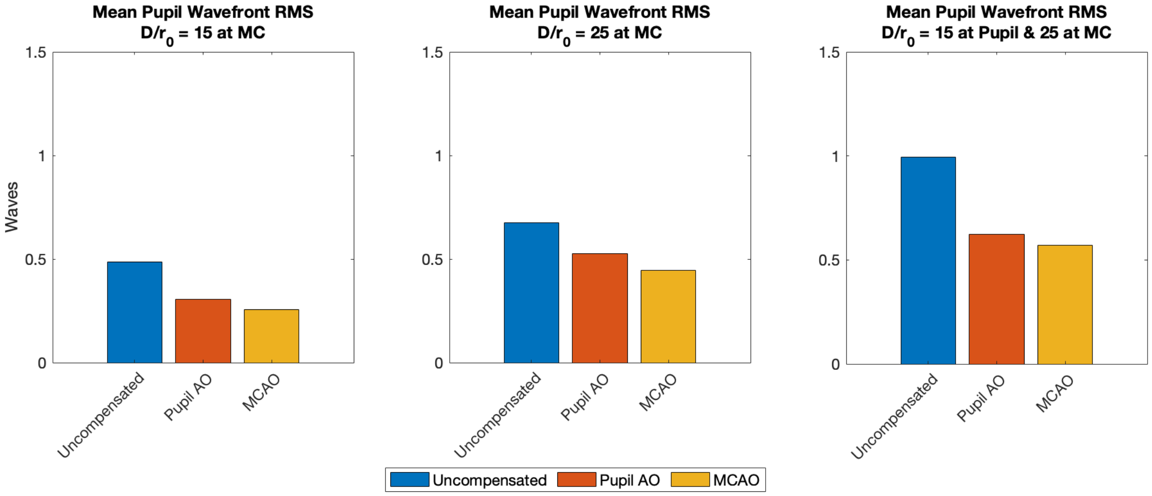

Figure 30. Mean pupil wavefront root mean squared error

D. PUPIL INTENSITY ANALYSIS

This section analyzes the effects of pupil AO and MCAO on pupil image intensity. It presents an example of pupil image intensity effects using the two AO techniques. The effectiveness of this compensation is quantified by pupil plane log-amplitude variance, which characterizes the degree of scintillation across the beam. Additionally, the pupil power in the bucket (PIB) is analyzed to assess AO effects on the transmitted beam power.

Figure 31 shows an example of AO compensation progression for a turbulence simulation run using the phase plate equivalent to $D/r_0 = 15$ at the pupil plane and $D/r_0 = 25$ at the multi-conjugate plane. This example illustrates the extraordinarily subtle nature of the scintillation change observed in the captured pupil plane images. It is difficult to visually ascertain much difference outside of a direct comparison on a high-resolution video monitor. This highlights why computing the log-amplitude variance of the intensities across these images can help pull out the details that are not clear in the images alone.

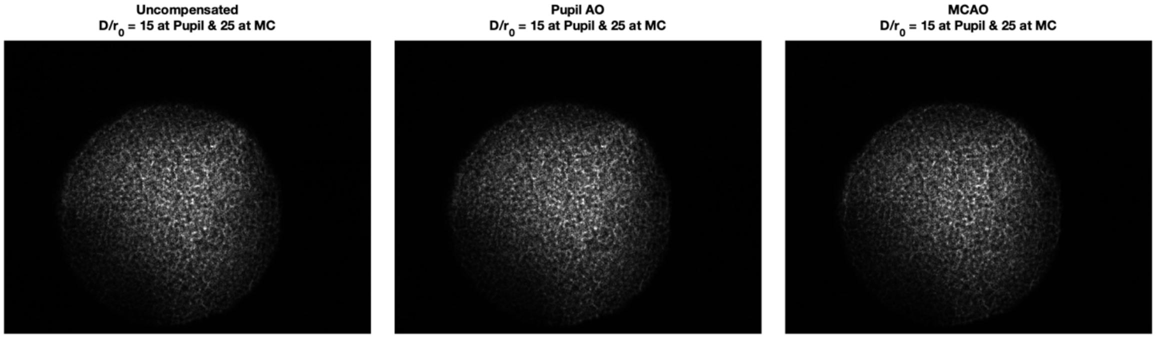

Figure 31. Pupil image compensation progression, severe case

Figure 32 graphs the pupil intensity log-amplitude variance measured under the turbulence conditions and compensation methods tested. As the turbulence conditions become more severe, there is a corresponding increase in pupil intensity scintillation, as expected. The application of Pupil AO and MCAO methods certainly changes the log-amplitude variance, confirming that pupil plane scintillation can be influenced by applying AO techniques. However, trends are difficult to ascertain in this figure alone.

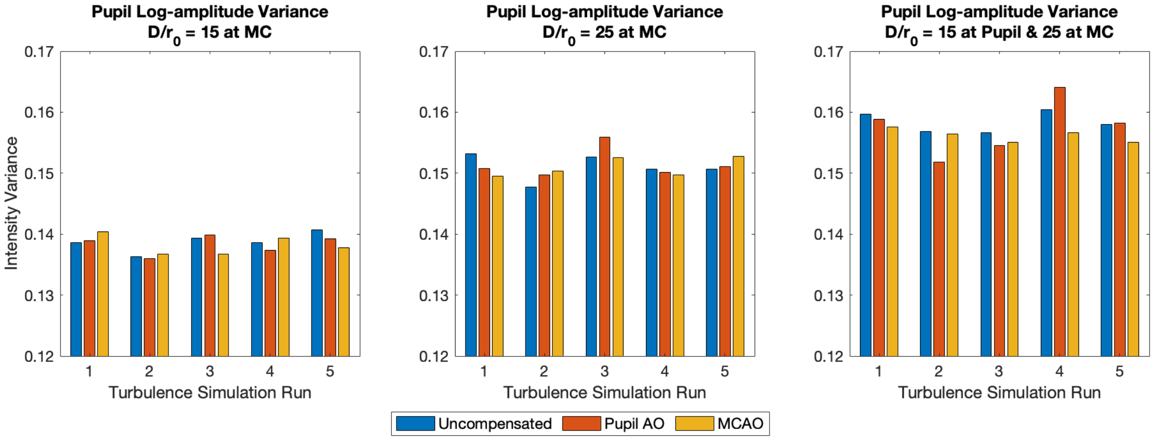

Figure 32. Measured pupil intensity log-amplitude variance

Figure 33 displays the mean pupil intensity log-amplitude variance across the five pseudorandom turbulence simulations at each turbulence level and compensation technique. This attempts to derive a trend in the influence of the two AO techniques, particularly MCAO, on pupil scintillation. Figure 33 shows that, generally, the variance was only marginally influenced by either pupil AO or MCAO at the two less turbulent levels. Only at the most severe deep turbulence level simulated, $D/r_0 = 15$ at the pupil plane and $D/r_0 = 25$ at the multi-conjugate plane, can a clear trend towards improvement be seen. This suggests that under severe deep turbulence conditions, MCAO does reduce scintillation in the pupil plane. However, more extensive testing and optimization would need to be performed to characterize better the degree to which MCAO can compensate for pupil scintillation and whether a similar result can be achieved under lesser deep turbulence conditions.

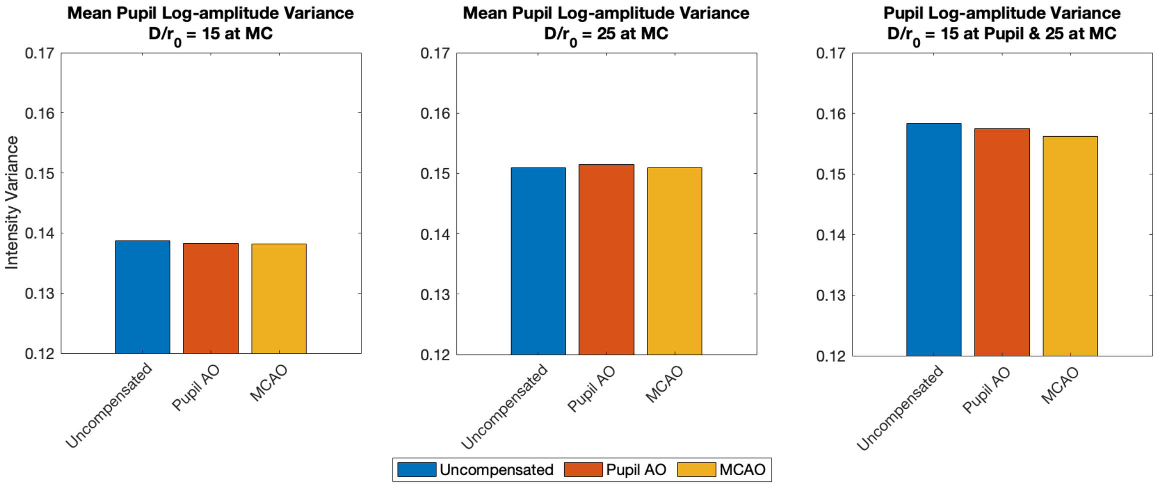

Figure 33. Mean pupil intensity log-amplitude variance

Figure 34 graphs the pupil power in the bucket (PIB) across each turbulence condition and compensation method we tested. PIB refers to the sum of the intensities of the pixels in the captured pupil images. These results suggest no significant correlation between turbulence level and the total power measured at the pupil aperture.

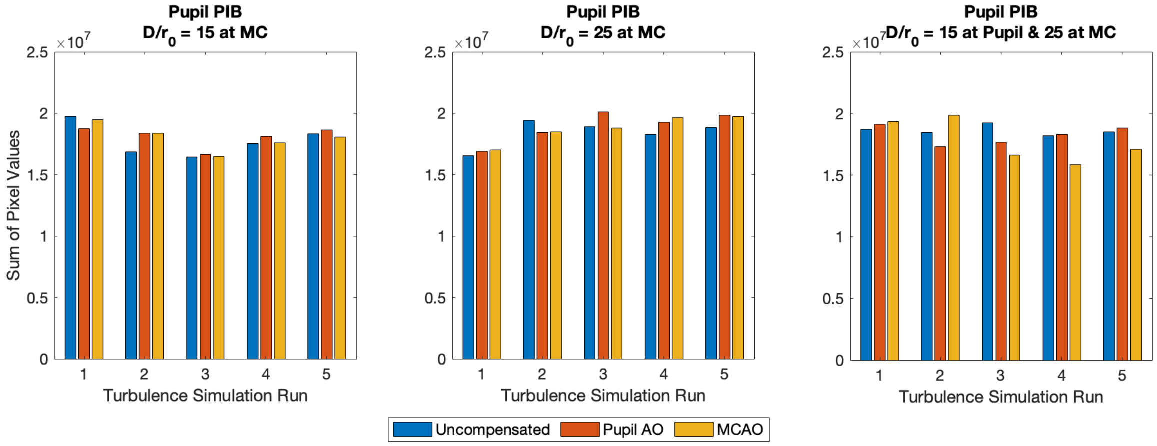

Figure 34. Measured pupil image power-in-the-bucket

Figure 35 shows the mean PIB across the experimental configurations. Pupil AO and MCAO do not significantly change the measured pupil PIB. This indicates that power transmission is generally maintained, albeit spread over a wide range of scintillation peaks and troughs rather than spread across uniform intensity. The severe turbulence conditions tested in this experiment led to unexpectedly large intensity peaks across the pupil image, in some instances reaching the saturation limit of the camera. For this reason, the measured PIB likely does not account for the entire sum of power within the pupil in all cases. This may account for the decreasing trend seen in the most severe deep turbulence case.

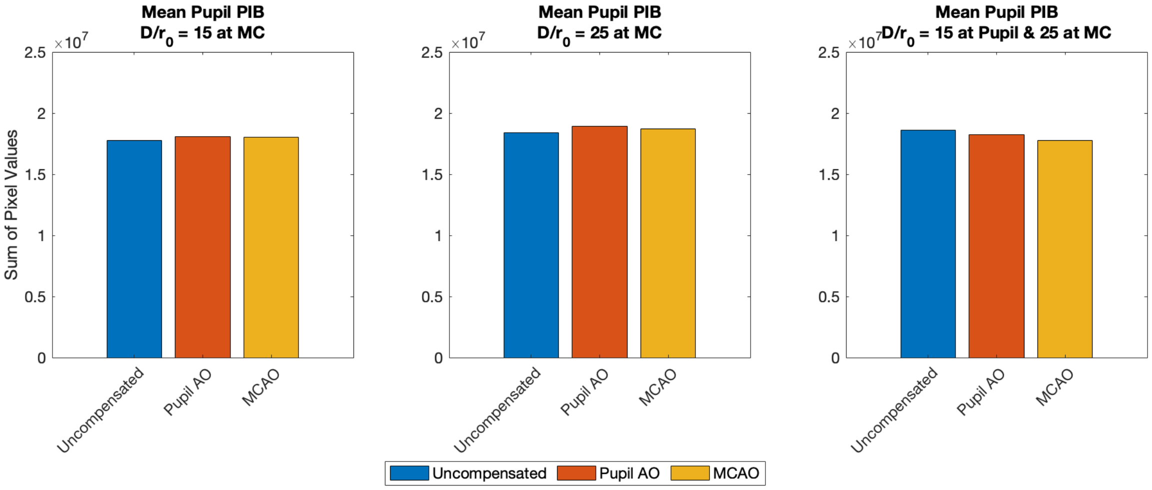

Figure 35. Mean pupil image power-in-the-bucket

THIS PAGE INTENTIONALLY LEFT BLANK

V. CONCLUSIONS AND FUTURE WORK

A. WAVEFRONT ABERRATION COMPENSATION PERFORMANCE

The research presented in this thesis experimentally confirmed that using two DMs conjugated to two different planes along the deep turbulence path can reduce more wavefront errors and significantly improve a propagating laser beam's PSF compared to single-DM AO. This is evidenced by an average improvement in PSF peak intensity of at least 28% over pupil AO alone and, in some cases, much more. Improving PSF peak intensity is vital for placing more optical energy on target. This could enable improved performance of laser and imaging systems at increased range. Wavefront error improvement was not as evident as PSF improvement due to the limitations of the pupil plane Shack-Hartmann sensor used in the experiment. The additional DM in the optical path also helped to increase the spatial frequency of the wavefront error that the AO system could correct.

B. SCINTILLATION PERFORMANCE

This research experimentally showed that using DMs to correct phase at two separate conjugate planes can reduce beam scintillation under the harshest simulated deep turbulence conditions. The experimental results showed only modest improvements in compensating scintillation at the pupil plane because the residual wavefront error after the multi-conjugate DM correction still induced significant scintillation. These results suggest that scintillation compensation demands better compensation of wavefront error at the muti-conjugate plane even though the system achieved much improved wavefront aberration and PSF compensation performance. While the two-DM system was better than the single-DM system, meaningful scintillation compensation may require additional DMs to further reduce the wavefront error along the optical path.

C. FUTURE WORK

The complexity of the testbed and physical considerations for laboratory work limited the experimental work conducted as part of this research. Implementing a MCAO system in a realistic scenario would be much more difficult because deep turbulence does not happen at two planes alone for horizontal beam propagation. Instead, it is continuous all along the column of the propagation path. In other words, the turbulence planes are infinite, and one would need an infinite number of DMs, each conjugate to its own plane, to achieve perfect compensations. While that prospect is impossible, exploring the optimization of two or more DMs when dealing with more realistic turbulence conditions is possible. To this end, future efforts might focus on placing the DMs slightly off the pupil or multi-conjugate planes.

There is also room to improve the NPS MCAO testbed itself. The operator must interface with multiple software components to run experiments as configured. If the sensors, DMs, cameras, and rotary stages were controlled through one shared MATLAB interface, it could significantly reduce the time needed to collect data points. Better integration of the testbed components could increase the amount of data points collected in future experiments, offering greater insight into MCAO performance.

APPENDIX A. EXPERIMENTAL DATA MATRIX

Table 1. MCAO experiment data point collection matrix

Test ID	Turbulence Condition	Wheel Rotation	Correction Applied	PSF Image	Pupil Image	Pupil WFS Image (FS)	Pupil WF Plot (FS)	MC WFS Image (ML)	MC Slope Calculation (ML)
1.1.1	No Plate	n/a	No	x	x	x	x	x	x
1.1.2	No Plate	n/a	Pupil	x	x	x	x	x	x
1.1.3	No Plate	n/a	Pupil + MC	x	x	x	x	x	x
2.1.1	D/r0 = 15 @ MC	1	No	x	x	x	x	x	x
2.1.2	D/r0 = 15 @ MC	1	Pupil	x	x	x	x	x	x
2.1.3	D/r0 = 15 @ MC	1	Pupil + MC	x	x	x	x	x	x
2.2.1	D/r0 = 15 @ MC	2	No	x	x	x	x	x	x
2.2.2	D/r0 = 15 @ MC	2	Pupil	x	x	x	x	x	x
2.2.3	D/r0 = 15 @ MC	2	Pupil + MC	x	x	x	x	x	x
2.3.1	D/r0 = 15 @ MC	3	No	x	x	x	x	x	x
2.3.2	D/r0 = 15 @ MC	3	Pupil	x	x	x	x	x	x
2.3.3	D/r0 = 15 @ MC	3	Pupil + MC	x	x	x	x	x	x
2.4.1	D/r0 = 15 @ MC	4	No	x	x	x	x	x	x
2.4.2	D/r0 = 15 @ MC	4	Pupil	x	x	x	x	x	x
2.4.3	D/r0 = 15 @ MC	4	Pupil + MC	x	x	x	x	x	x
2.5.1	D/r0 = 15 @ MC	5	No	x	x	x	x	x	x
2.5.2	D/r0 = 15 @ MC	5	Pupil	x	x	x	x	x	x
2.5.3	D/r0 = 15 @ MC	5	Pupil + MC	x	x	x	x	x	x
3.1.1	D/r0 = 25 @ MC	1	No	x	x	x	x	x	x
3.1.2	D/r0 = 25 @ MC	1	Pupil	x	x	x	x	x	x
3.1.3	D/r0 = 25 @ MC	1	Pupil + MC	x	x	x	x	x	x
3.2.1	D/r0 = 25 @ MC	2	No	x	x	x	x	x	x
3.2.2	D/r0 = 25 @ MC	2	Pupil	x	x	x	x	x	x
3.2.3	D/r0 = 25 @ MC	2	Pupil + MC	x	x	x	x	x	x
3.3.1	D/r0 = 25 @ MC	3	No	x	x	x	x	x	x
3.3.2	D/r0 = 25 @ MC	3	Pupil	x	x	x	x	x	x
3.3.3	D/r0 = 25 @ MC	3	Pupil + MC	x	x	x	x	x	x
3.4.1	D/r0 = 25 @ MC	4	No	x	x	x	x	x	x
3.4.2	D/r0 = 25 @ MC	4	Pupil	x	x	x	x	x	x
3.4.3	D/r0 = 25 @ MC	4	Pupil + MC	x	x	x	x	x	x
3.5.1	D/r0 = 25 @ MC	5	No	x	x	x	x	x	x
3.5.2	D/r0 = 25 @ MC	5	Pupil	x	x	x	x	x	x
3.5.3	D/r0 = 25 @ MC	5	Pupil + MC	x	x	x	x	x	x
4.1.1	D/r0 = 25 @ MC + 15 @ P	1	No	x	x	x	x	x	x
4.1.2	D/r0 = 25 @ MC + 15 @ P	1	Pupil	x	x	x	x	x	x
4.1.3	D/r0 = 25 @ MC + 15 @ P	1	Pupil + MC	x	x	x	x	x	x
4.2.1	D/r0 = 25 @ MC + 15 @ P	2	No	x	x	x	x	x	x
4.2.2	D/r0 = 25 @ MC + 15 @ P	2	Pupil	x	x	x	x	x	x
4.2.3	D/r0 = 25 @ MC + 15 @ P	2	Pupil + MC	x	x	x	x	x	x
4.3.1	D/r0 = 25 @ MC + 15 @ P	3	No	x	x	x	x	x	x
4.3.2	D/r0 = 25 @ MC + 15 @ P	3	Pupil	x	x	x	x	x	x
4.3.3	D/r0 = 25 @ MC + 15 @ P	3	Pupil + MC	x	x	x	x	x	x
4.4.1	D/r0 = 25 @ MC + 15 @ P	4	No	x	x	x	x	x	x
4.4.2	D/r0 = 25 @ MC + 15 @ P	4	Pupil	x	x	x	x	x	x
4.4.3	D/r0 = 25 @ MC + 15 @ P	4	Pupil + MC	x	x	x	x	x	x
4.5.1	D/r0 = 25 @ MC + 15 @ P	5	No	x	x	x	x	x	x
4.5.2	D/r0 = 25 @ MC + 15 @ P	5	Pupil	x	x	x	x	x	x
4.5.3	D/r0 = 25 @ MC + 15 @ P	5	Pupil + MC	x	x	x	x	x	x

Table 2. MCAO experiment calculation results matrix

Test ID	Turbulence Condition	Wheel Rotation	Correction Applied	PSF Peak Intensity	Pupil Mean Intensity	Pupil NIV	log-amp Variance	Pupil Power in Bucket	Pupil Peak-to-valley	Pupil RMS	Pupil Strehl
1.1.1	No Plate	n/a	No	255	38.262969	3.11E-06	0.10121003	17356121	0.835	0.075	0.759
1.1.2	No Plate	n/a	Pupil	255	36.7906618	3.12E-06	0.10310869	16688281	0.614	0.077	0.744
1.1.3	No Plate	n/a	Pupil + MC	255	38.4532838	3.10E-06	0.10114848	17442448	2	0.134	0.529
2.1.1	D/r0 = 15 @ MC	1	No	161	43.4632618	3.53E-06	0.13856804	19714979	3.685	0.513	0.004
2.1.2	D/r0 = 15 @ MC	1	Pupil	193	41.3028256	3.53E-06	0.13887459	18735003	4.619	0.361	0.048
2.1.3	D/r0 = 15 @ MC	1	Pupil + MC	255	42.9784436	3.53E-06	0.14039217	19495065	2.963	0.317	0.008
2.2.1	D/r0 = 15 @ MC	2	No	145	37.167687	3.53E-06	0.13634338	16859300	4.761	0.536	0.007
2.2.2	D/r0 = 15 @ MC	2	Pupil	255	40.4443884	3.51E-06	0.13594854	18345615	5.22	0.29	0.302
2.2.3	D/r0 = 15 @ MC	2	Pupil + MC	255	40.5095161	3.52E-06	0.13668029	18375157	2.36	0.298	0.121
2.3.1	D/r0 = 15 @ MC	3	No	94	36.2686745	3.60E-06	0.13937099	16451507	4.641	0.483	0.002
2.3.2	D/r0 = 15 @ MC	3	Pupil	156	36.7154349	3.58E-06	0.13985613	16654158	2.424	0.275	0.075
2.3.3	D/r0 = 15 @ MC	3	Pupil + MC	255	36.3895252	3.56E-06	0.13672634	16506325	1.661	0.23	0.049
2.4.1	D/r0 = 15 @ MC	4	No	148	38.6562728	3.56E-06	0.1386578	17534524	3.33	0.535	0.001
2.4.2	D/r0 = 15 @ MC	4	Pupil	208	39.8863142	3.55E-06	0.13734656	18092472	2.783	0.359	0.043
2.4.3	D/r0 = 15 @ MC	4	Pupil + MC	255	38.7774564	3.57E-06	0.13929415	17589493	1.992	0.204	0.149
2.5.1	D/r0 = 15 @ MC	5	No	151	40.4143686	3.54E-06	0.14073604	18331998	3.029	0.363	0.008
2.5.2	D/r0 = 15 @ MC	5	Pupil	180	41.110617	3.53E-06	0.13919487	18647817	1.576	0.245	0.05
2.5.3	D/r0 = 15 @ MC	5	Pupil + MC	255	39.7678643	3.53E-06	0.13781365	18038743	2.65	0.234	0.134
3.1.1	D/r0 = 25 @ MC	1	No	48	36.4679575	3.81E-06	0.15314188	16541902	4.399	0.618	0.005
3.1.2	D/r0 = 25 @ MC	1	Pupil	85	37.2195762	3.80E-06	0.1507727	16882837	3.512	0.505	0.024
3.1.3	D/r0 = 25 @ MC	1	Pupil + MC	216	37.4439408	3.78E-06	0.14950422	16984609	5.466	0.452	0.01
3.2.1	D/r0 = 25 @ MC	2	No	71	42.7544472	3.73E-06	0.14773024	19393460	4.323	0.627	0.011
3.2.2	D/r0 = 25 @ MC	2	Pupil	95	40.6129815	3.76E-06	0.14970682	18422089	5.784	0.472	0.03
3.2.3	D/r0 = 25 @ MC	2	Pupil + MC	255	40.7094583	3.76E-06	0.1503238	18465851	3.029	0.383	0.024
3.3.1	D/r0 = 25 @ MC	3	No	73	41.6893195	3.78E-06	0.15263249	18910317	6.108	0.746	0.005
3.3.2	D/r0 = 25 @ MC	3	Pupil	70	44.3420142	3.79E-06	0.15588808	20113582	3.447	0.585	0.004
3.3.3	D/r0 = 25 @ MC	3	Pupil + MC	255	41.4006649	3.79E-06	0.15249696	18779383	6.687	0.547	0.049
3.4.1	D/r0 = 25 @ MC	4	No	77	40.2895232	3.77E-06	0.15062234	18275368	2.817	0.559	0.006
3.4.2	D/r0 = 25 @ MC	4	Pupil	109	42.4343465	3.76E-06	0.15016216	19248262	4.776	0.39	0.003
3.4.3	D/r0 = 25 @ MC	4	Pupil + MC	255	43.285674	3.74E-06	0.14974549	19634425	6.453	0.347	0.043
3.5.1	D/r0 = 25 @ MC	5	No	63	41.5422541	3.80E-06	0.15068611	18843608	7.037	0.827	0
3.5.2	D/r0 = 25 @ MC	5	Pupil	95	43.7280958	3.80E-06	0.15106789	19835108	6.389	0.673	0.049
3.5.3	D/r0 = 25 @ MC	5	Pupil + MC	219	43.5019985	3.78E-06	0.15279145	19732550	4.388	0.5	0.004
4.1.1	D/r0 = 25 @ MC + 15 @ P	1	No	70	41.285103	3.88E-06	0.1596919	18726964	5.233	0.664	0.001
4.1.2	D/r0 = 25 @ MC + 15 @ P	1	Pupil	56	42.1594529	3.88E-06	0.158811	19123570	5.355	0.598	0.001
4.1.3	D/r0 = 25 @ MC + 15 @ P	1	Pupil + MC	132	42.5742999	3.86E-06	0.15756917	19311745	9.188	0.673	0.03
4.2.1	D/r0 = 25 @ MC + 15 @ P	2	No	38	40.6776484	3.84E-06	0.15680936	18451422	19.587	1.44	0.001
4.2.2	D/r0 = 25 @ MC + 15 @ P	2	Pupil	47	38.0871074	3.83E-06	0.1518417	17276350	6.261	0.645	0
4.2.3	D/r0 = 25 @ MC + 15 @ P	2	Pupil + MC	136	43.7880869	3.85E-06	0.15647656	19862320	5.814	0.648	0.013
4.3.1	D/r0 = 25 @ MC + 15 @ P	3	No	63	42.3961345	3.87E-06	0.15664055	19230929	6.629	0.9	0
4.3.2	D/r0 = 25 @ MC + 15 @ P	3	Pupil	37	38.9157784	3.87E-06	0.1545174	17652236	3.959	0.481	0.023
4.3.3	D/r0 = 25 @ MC + 15 @ P	3	Pupil + MC	119	36.6740836	3.89E-06	0.15508729	16635401	4.914	0.57	0.03
4.4.1	D/r0 = 25 @ MC + 15 @ P	4	No	35	40.1151827	3.91E-06	0.16039341	18196287	5.994	0.687	0.001
4.4.2	D/r0 = 25 @ MC + 15 @ P	4	Pupil	40	40.3075633	3.94E-06	0.16403391	18283551	5.451	0.618	0.01
4.4.3	D/r0 = 25 @ MC + 15 @ P	4	Pupil + MC	76	34.8993366	3.92E-06	0.15661086	15830374	9.252	0.619	0.013
4.5.1	D/r0 = 25 @ MC + 15 @ P	5	No	55	40.7554238	3.88E-06	0.15796976	18486701	11.161	1.273	0.013
4.5.2	D/r0 = 25 @ MC + 15 @ P	5	Pupil	80	41.5060902	3.89E-06	0.15825292	18827204	9.69	0.777	0.002
4.5.3	D/r0 = 25 @ MC + 15 @ P	5	Pupil + MC	255	37.7050602	3.88E-06	0.15506285	17103053	2.939	0.347	0.053

APPENDIX B. MCAO TESTBED SOFTWARE PARAMETERS

This Appendix contains the technical parameters of the NPS MCAO testbed. It outlines the specific settings used in the various software programs to perform the experimental portion of this research. Table 3 enumerates the serial numbers of the various testbed sensors often used to interact with and configure them.

Table 3. MCAO tested camera serial numbers

Camera	Serial No.
PSF	4103177612
Pupil	4103177606
Pupil WFS	4103177607
MCAO WFS	4103607483

Figures 36 and 37 are screenshots of the uEye camera settings used to capture the pupil and PSF images for this research. It is important to note that the gain settings for these cameras should be set to zero to avoid noise in the captured images.

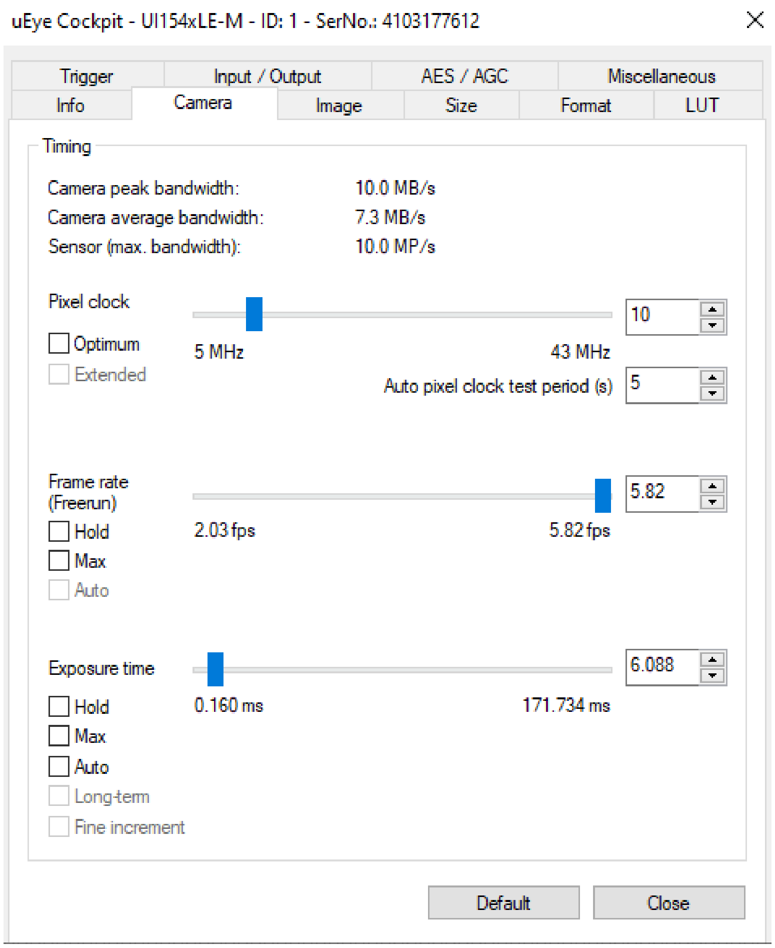

Timing

Camera peak bandwidth: 10.0 MB/s
Camera average bandwidth: 7.3 MB/s
Sensor (max. bandwidth): 10.0 MP/s

Pixel clock: 10 (5 MHz – 43 MHz)
☐ Optimum
☐ Extended
Auto pixel clock test period (s): 5

Frame rate (Freerun): 5.82 (2.03 fps – 5.82 fps)
☐ Hold
☐ Max
☐ Auto

Exposure time: 6.088 (0.160 ms – 171.734 ms)
☐ Hold
☐ Max
☐ Auto
☐ Long-term
☐ Fine increment

Figure 36. PSF camera data acquisition settings

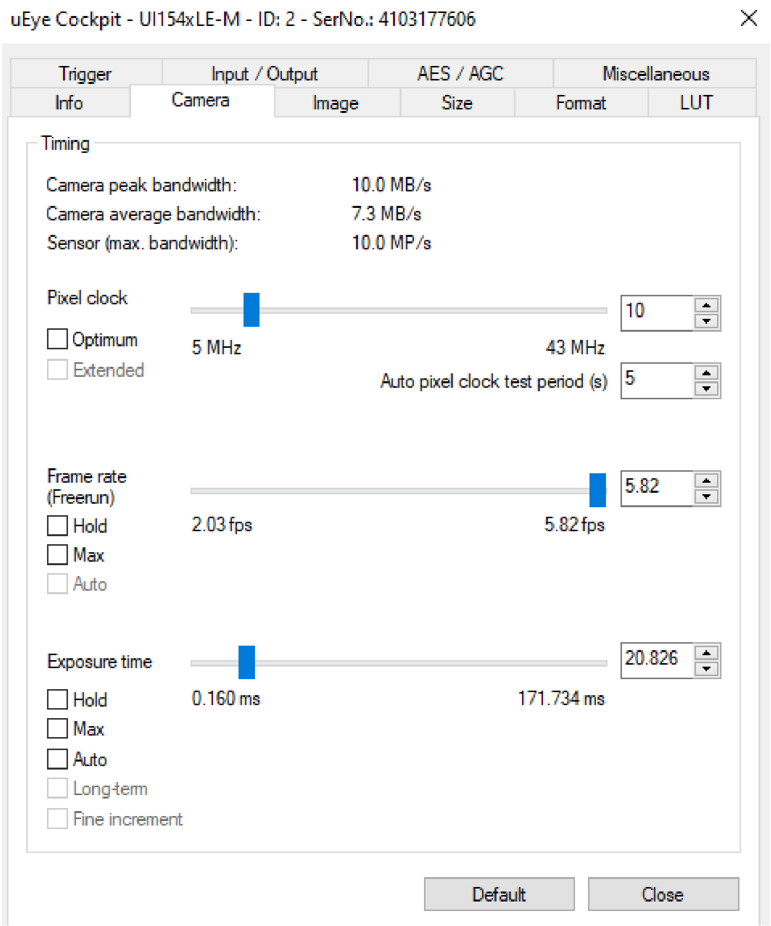

uEye Cockpit - UI154xLE-M - ID: 2 - SerNo.: 4103177606

Timing

Camera peak bandwidth: 10.0 MB/s
Camera average bandwidth: 7.3 MB/s
Sensor (max. bandwidth): 10.0 MP/s

Pixel clock: 10 (5 MHz – 43 MHz)
☐ Optimum
☐ Extended
Auto pixel clock test period (s): 5

Frame rate (Freerun): 5.82 (2.03 fps – 5.82 fps)
☐ Hold
☐ Max
☐ Auto

Exposure time: 20.826 (0.160 ms – 171.734 ms)
☐ Hold
☐ Max
☐ Auto
☐ Long-term
☐ Fine increment

Figure 37. Pupil camera data acquisition settings

Figure 38 is a screenshot of the Shack-Hartmann paraments that must be correctly set in FrontSurfer. These parameters reflect the physical characteristics of the OKO Shack-Hartmann wavefront sensor used at the pupil plane.

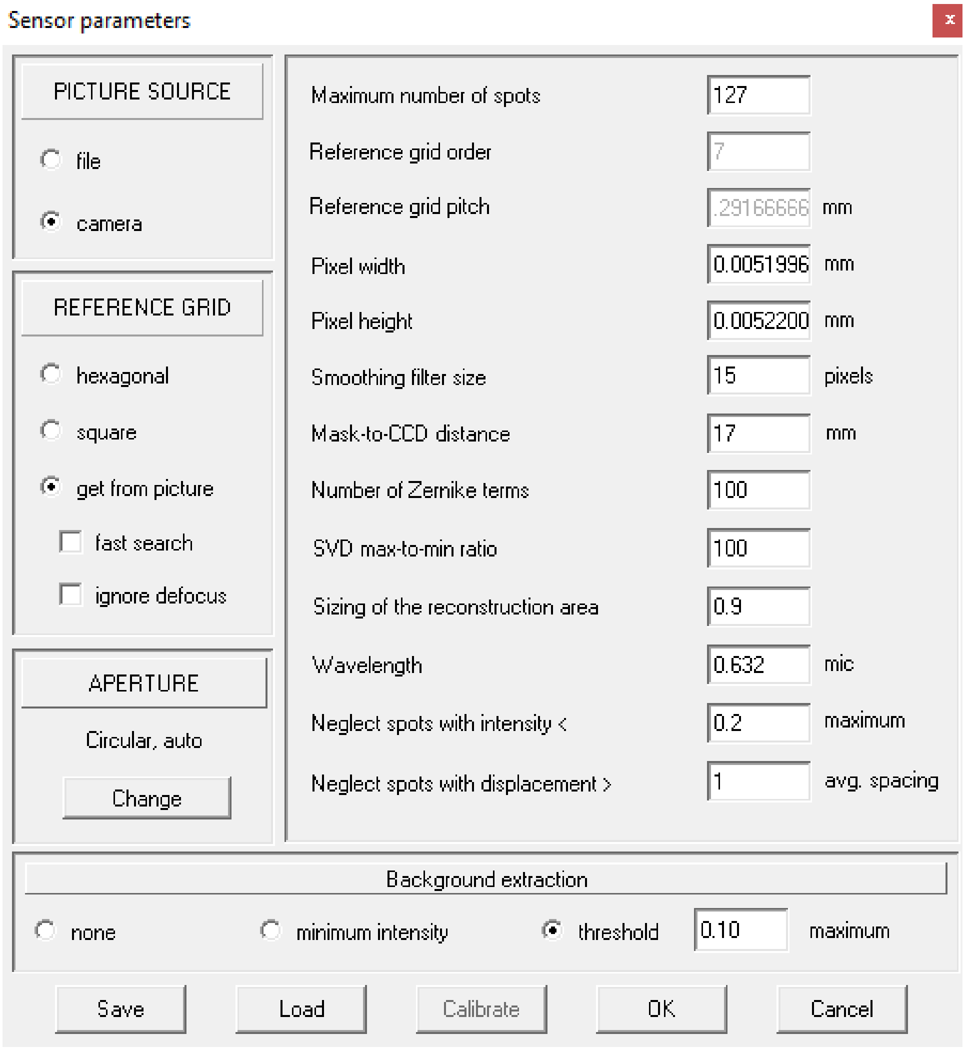

Sensor parameters

PICTURE SOURCE

○ file

● camera

REFERENCE GRID

○ hexagonal

○ square

● get from picture

☐ fast search

☐ ignore defocus

APERTURE

Circular, auto

Maximum number of spots	127	
Reference grid order	7	
Reference grid pitch	.29166666	mm
Pixel width	0.0051996	mm
Pixel height	0.0052200	mm
Smoothing filter size	15	pixels
Mask-to-CCD distance	17	mm
Number of Zernike terms	100	
SVD max-to-min ratio	100	
Sizing of the reconstruction area	0.9	
Wavelength	0.632	mic
Neglect spots with intensity <	0.2	maximum
Neglect spots with displacement >	1	avg. spacing

Background extraction

○ none ○ minimum intensity ● threshold 0.10 maximum

Figure 38. Pupil Shack-Hartmann parameters in FrontSurfer

Figure 39 shows a screenshot of the camera properties used in FrontSurfer for the pupil Shack-Hartmann wavefront sensor. The exposure setting was particularly critical for ensuring that the spots in the sensor were neither too dark nor too bright. A proper exposure ensures that the sensor can best measure the wavefront and close the feedback control loop to the pupil DM.

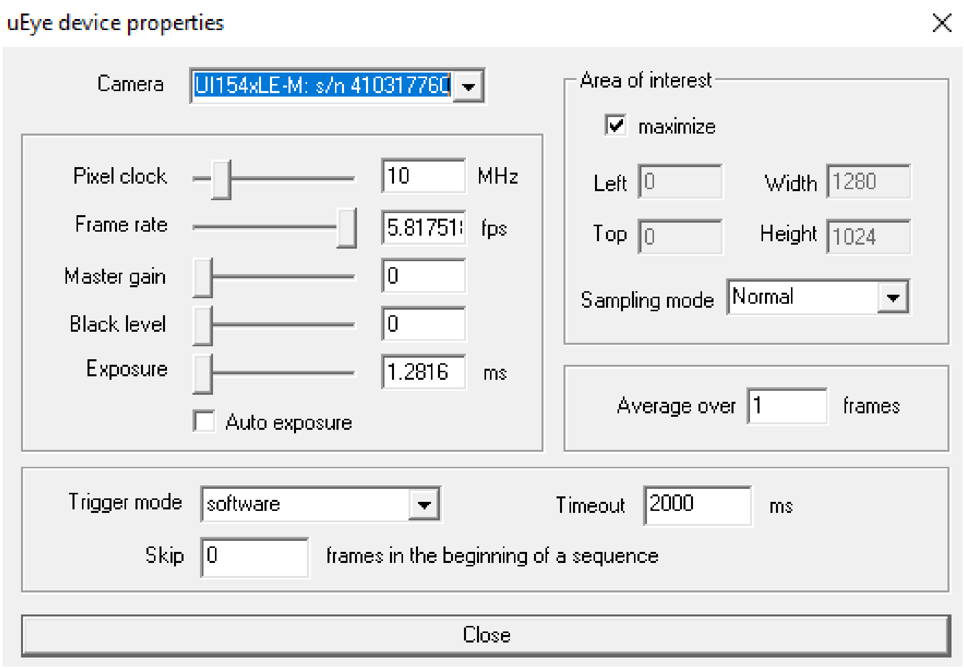

Camera: UI154xLE-M: s/n 410317760

Pixel clock: 10 MHz

Frame rate: 5.81751 fps

Master gain: 0

Black level: 0

Exposure: 1.2816 ms

☐ Auto exposure

☑ maximize

Left: 0

Width: 1280

Top: 0

Height: 1024

Sampling mode: Normal

Average over 1 frames

Trigger mode: software

Timeout: 2000 ms

Skip 0 frames in the beginning of a sequence

Figure 39. Pupil WFS camera properties in FrontSurfer

Figure 40 shows a screenshot of the feedback parameters used in the FrontSurfer software to control the pupil DM. The voltage steps and feedback parameters are critical drivers of pupil DM performance. The parameters used in this research reflect those the pupil DM manufacturer recommended.

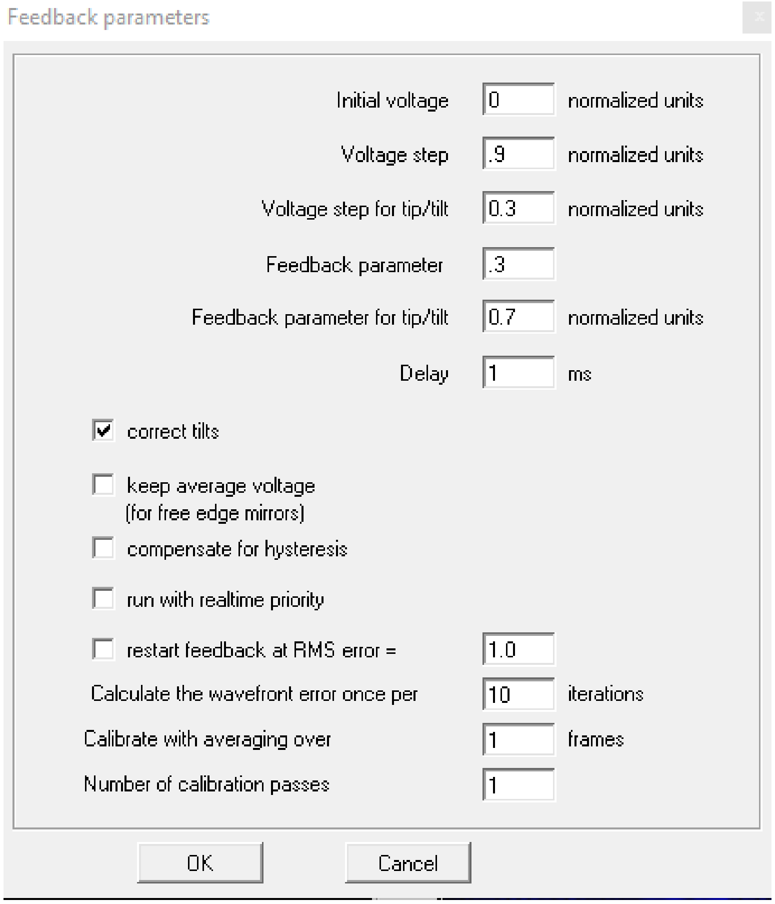

Feedback parameters

Initial voltage 0 normalized units

Voltage step .9 normalized units

Voltage step for tip/tilt 0.3 normalized units

Feedback parameter .3

Feedback parameter for tip/tilt 0.7 normalized units

Delay 1 ms

☑ correct tilts

☐ keep average voltage (for free edge mirrors)

☐ compensate for hysteresis

☐ run with realtime priority

☐ restart feedback at RMS error = 1.0

Calculate the wavefront error once per 10 iterations

Calibrate with averaging over 1 frames

Number of calibration passes 1

Figure 40. Pupil DM control feedback parameters

APPENDIX C. MATLAB MCAO PRIMARY CONTROL CODE

```
%%
% clear all
clear all;close all;

%% initialize DM
[s,port] = serialParameter; % DM Serial port
DM_status = DM_power_up(s); % DM power up
disp('DM powered up, wait till the driver reaches to the bias voltage and hit enter to continue');
%pause;

%% initialize SHWFS camera
vidobj = videoinput('winvideo', 4,'UYVY_1280x1024'); % may need to change number 1–4
vidobj.ReturnedColorSpace = 'grayscale';

% Access the currently selected video source object
src = getselectedsource(vidobj);
src.ExposureMode = 'manual';
src.BrightnessMode = 'manual';
src.ContrastMode = 'manual';
src.GainMode = 'manual';
src.Exposure = -9.5;
%preview(vidobj);
frame = getsnapshot(vidobj);
figure(1);imshow(frame);colormap gray;hold on;

%% load reference grid and dark map
load refernce_images
load box_grid

[X,Y] = meshgrid(0:24,0:24);
frame_ref = SH_reference-dark;
for j = 1:465
  % compute centroid for each SH spot
  sub_roi = frame_ref(box_grid(j,2)-12:box_grid(j,2)+12,box_grid(j,1)-12:box_grid(j,1)+12);
  sub_roi = double(sub_roi);
  cX = sum(sub_roi.*X)/sum (sub_roi);
  cY = sum(sub_roi.*Y)/sum (sub_roi);
  SH_spot_ref(j,:) = [box_grid(j,1)-12+cX box_grid(j,2)-12+cY];
  %rectangle('Position',[box_grid(j,1)-12 box_grid(j,2)-12 25 25], 'EdgeColor', [1 1 1]);
  %plot(SH_spot_ref(j,1),SH_spot_ref(j,2),'+')
end

%% load poke inverse
```

```
load('poke_matrix_inv.mat');

%% control loop starts here
u_349 = zeros(349,1); % initial control command
update_rate = 5;

for i = 1:30
  i
  % measure SH spots
  frame = getsnapshot(vidobj)-dark;
  for j = 1:465
      % compute centroid for each SH spot
      sub_roi = frame(box_grid(j,2)-12:box_grid(j,2)+12,box_grid(j,1)-12:box_grid(j,1)+12);
      sub_roi = double(sub_roi);
      cX = sum(sub_roi.*X)/sum (sub_roi);
      cY = sum(sub_roi.*Y)/sum (sub_roi);
      SH_spot(j,:) = [box_grid(j,1)-12+cX box_grid(j,2)-12+cY];
      %rectangle('Position',[box_grid(j,1)-12 box_grid(j,2)-12 25 25], 'EdgeColor', [1 1 1]);
      %plot(SH_spot_p(j,1),SH_spot_p(j,2),'+')
  end
  u_349 = u_349-update_rate*poke_matrix_inv*([SH_spot(:,1);SH_spot(:,2)]-
[SH_spot_ref(:,1);SH_spot_ref(:,2)]);
  u_349 = u_349 – mean(u_349);
  u_349(find(u_349>=20)) = 20; % limit voltage to +-15V
  u_349(find(u_349<=-20)) = -20; % limit voltage to +-15V
  u_441 = convert349to441(u_349);
  DM_status = DM_update(s,u_441);
end

%% Reset control
u_349 = zeros(349,1); % reset control
u_441 = convert349to441(u_349);
DM_status = DM_update(s,u_441);

%% Reset camera
delete(vidobj);
clear("vidobj");
clear("src");
imaqreset;

%% DM Power down
DM_status = DM_power_down(s)

%% Clear connections
clear s
```

LIST OF REFERENCES

[1] L. C. Andrews, *Field Guide to Atmospheric Optics*, 2nd Ed. (SPIE Field Guides, vol. FG41). Bellingham, WA, USA: SPIE Press, 2019.

[2] P. N. Crabtree, "Multi-Conjugate Adaptive Optics for the Compensation of Amplitude and Phase Distortions," M.S. thesis, Dept. of Elec. Eng., Air Force Institute of Technology, Wright-Patterson Air Force Base, OH, USA, 2000.

[3] M. S. Corley, "Maritime Adaptive Optics Beam Control," Ph.D. dissertation, Dept. of Mech. and Aero. Eng., Naval Postgraduate School, Monterey, CA, USA, 2010.

[4] P. Sprangle *et al.*, "Beacon Beams for Deep Turbulence High Energy Laser Beam Directors." Naval Research Laboratory, Plasma Physics Division, Washington DC, USA, Nov. 02, 2012.

[5] J. J. Kim, "Beam Propagation Through Atmosphere," presented at the AE4818 Acquisition, Tracking, and Pointing of Military Spacecraft Course, Monterey, CA, USA, 2022.

[6] J. Andrews *et al.*, "Using Two MEMS Deformable Mirrors in an Adaptive Optics Test Bed for Multi-Conjugate Correction," in *SPIE MOEMS-MEMS*, San Francisco, CA, USA, 2010.

[7] S. Restaino *et al.*, "Multi-Conjugate Adaptive Optics Test-bed for Horizontal Propagation." Naval Research Laboratory, Remote Sensing Division, Washington DC, USA, Sep. 2010.

[8] J. J. Kim, "Project Progress: Advanced Adaptive Optics and Jitter Control Methods with Integrated Beam Control Experiments," presented at the Office of Naval Research Science & Technology Progress Update, Monterey, CA, USA, Nov. 28, 2022.

[9] Kinetic Systems Inc., "Ultimate Grade – 5300 Series Optical Tables." Accessed: Sep. 17, 2023. Available: https://kineticsystems.com/products/optical-tables/ultimate-grade-5300-series-optical-tables/

[10] Lumentum, *Helium-Neon Laser Heads 1100 Series*, hnlh1100-ds-cl-ae. 2019. Available: https://resource.lumentum.com/s3fs-public/technical-library-items/hnlh1100_ds_cl_ae.pdf

[11] Lexitek Inc., *Turbulence Phase Plates*. 2018. Available: https://lexitek.com/pdfs/turbphasplat.pdf

[12] Lexitek Inc., *HS-100 Motorized Rotary Stage*. 2018. Available: https://lexitek.com/pdfs/HS-100%20Rotator.pdf

[13] Nippon Pulse America Inc., *PMX-4EX-SA Advanced 4-Axis Stepper Motion Controller*. 2018. Available: https://www.arcus-technology.com/products/multi-axis-motion-controller/4-axis-usb-controller/

[14] Flexible Optical BV, *96-Channel Deformable Mirror with Embedded Electronics*. 2022. Available: http://www.okotech.com/images/pdfs/mdm96_25.4_datasheet.pdf

[15] Northrop Grumman, *NPS 349 Channel Modular DM Acceptance Test Report*, D01-RE09106. 2021.

[16] Thorlabs Inc., "Shack-Hartmann Wavefront Sensors." Accessed: Sep. 20, 2023. Available: https://www.thorlabs.com/newgrouppage9.cfm?objectgroup_id=5287

[17] Flexible Optical BV, "Shack-Hartmann Standard Configurations." Accessed Sep. 17, 2023. Available: http://www.okotech.com/standard-configurations

[18] Edmund Optics, "25.0mm Diameter MgF2 Coated, Achromatic Lens Kit." Accessed: Oct. 15, 2023. Available: https://www.edmundoptics.com/p/250mm-diameter-mgfsub2sub-coated-achromatic-lens-kit/10590/

[19] IDS Imaging Development Systems GmbH, *UI-1540LE-M-GL Rev.2*. 2023. Available: https://www.ids-imaging.us/IDS/pdfsheet_pdf.php?sku=AB02536

INITIAL DISTRIBUTION LIST

1. Defense Technical Information Center
   Fort Belvoir, Virginia

2. Dudley Knox Library
   Naval Postgraduate School
   Monterey, California